CML

Computer Mechanics Laboratory

Technical Report No. 03-004

THE EFFECTS OF E-BLOCK ARM THICKNESS ON THE AIRFLOW DOWNSTREAM OF THE E-BLOCK ARM IN A MODELED HARD DISK DRIVE

Hany M. Gross, David B. Bogy, and Ömer Savas

Computer Mechanics Laboratory

Department of Mechanical Engineering

University of California, Berkeley 94720-1740

Toru Watanabe

HDD Division, Fujitsu Ltd.

4-4-1 Kamikodanaka, Nakahara-ku,

Kawasaki, 211-8588, Japan

January 2003

Abstract

The effects of E-block arm thickness on the airflow downstream of the E-block arm in a modeled hard disk drive were investigated. The primary objective of this work was to shed some light on head vibration results that were presented in an earlier study. Four different E-block arm thicknesses were used, ranging from 1.0 mm to 1.6 mm in steps of 0.2 mm. Airflow speed was measured in the region downstream of the arm tip using a constant-temperature hot-wire anemometer at the inner diameter radial position. The flow measurements were used to compute the mean and root mean square (rms) flow speed, the turbulence intensity, and the mean and rms dynamic pressure head distributions in the measurement region. The rms flow and dynamic pressure fluctuations were decomposed into components over several frequency bands. A correlation was observed between the dynamic pressure fluctuation components, and the corresponding components of the head off-track vibration. Clearly identifiable vortex shedding peaks were observed in the flow fluctuation power spectra.

Table of Contents

List of Tables

List of Figures

1. Introduction

The hard disk drive (HDD) industry is continually faced with demands for higher areal recording densities, faster data transfer rates, and higher reliability. The demand for a higher recording density translates directly into a demand for increasing the track density and/or the linear bit density, which, in turn, requires squeezing the track misregistration (TMR) and flying height modulation (FHM) into tighter budgets. On the other hand, the demand for higher data transfer rates and reduced latency dictates using faster disk rotation speeds. Such high disk speeds lead to greater flow velocities, and consequently to higher levels of aerodynamic forces in the drive.

In addition to controlling the temperature distribution and the concentration and transfer of particulates within the drive, the flow field in the drive and any large scale fluid structures it may contain constitute a significant disturbance to the read/write head motion, as they excite the structural modes of the head stack assembly (HSA) and of the disks, inducing TMR and FHM. As a result, it is of paramount importance to understand the nature and characteristics of the airflow in disk drives, as well as its impact on structural vibrations, if the performance of future drive generations is to be improved.

Investigations of the flow in disk drives have been carried out in configurations of varying degrees of geometric complexity. The fully-enshrouded assembly of co-rotating disks, with no obstructions inserted between the disks, is one of the simplest configurations considered, and was studied by several researchers including Lennemann

[1], Abrahamson *et al.* [2], Schuler *et al.* [3], Tzeng and Humphrey [4], and Humphrey et al [5]. Lennemann [1] used aluminum flake flow visualization in a water flow model and observed a laminar central core of fluid with a highly turbulent outer region. The core had a lobed or polygonal shape, extended from the hub to the periphery of the disks, and rotated at about 80 percent of the disk rotation speed. Abrahamson *et al.* [2] used a dye injection flow visualization technique in a water flow model and refined Lennemann's conclusions. They characterized the flow structure as consisting of three distinct regions. The first was an inner region dominated by rotation effects. This region moved in rigid body rotation, exhibiting little or no motion relative to the disks, and was observed to extend from the hub to approximately *75%* of the disk radius. The second region was a shroud boundary layer region, which was dominated by viscous effects due to the no-slip condition at the shroud wall. This region was observed to extend inward from the shroud to approximately 90 percent of the disk diameter. The third region was an outer region, which occupied the space between the inner region and the shroud boundary layer region. It experienced a mixture of rotational and viscous effects, which resulted in the formation of large, periodic, axially-aligned vortical structures that rotated counter to disk rotation. These vortices were polygonal in shape and nearly uniform in size, spanning the radial extent of the outer region. The inner and outer regions were both predominantly two-dimensional, whereas the shroud boundary layer region exhibited significant mean three-dimensional motion.

Schuler *et al.* [3] and Tzeng and Humphrey [4] experimentally investigated the airflow in the unobstructed space between a pair of disks using laser Doppler

anemometry (LDA). Their flow measurements along radial lines showed the flow to be divided into two main regions: an inner region in rigid body rotation whose mean flow speed was approximately equal to the local disk surface speed; and an outer region whose mean flow speed relative to the disk surface speed decreased linearly between the inner region and the disk edge. Their flow measurements along lines parallel to the spin axis revealed that the mean flow speed was fairly uniform along this direction.

Humphrey *et al.* [5] carried out numerical simulations to investigate the unsteady motion of the flow in the unobstructed space between a pair of fully-shrouded co-rotating disks. They performed two-dimensional (axisymmetric) and three-dimensional calculations in a configuration corresponding to the experimental setup employed by Schuler *et al.* [3]. Their two-dimensional simulations predicted that for Re < 22,200, the flow exhibited a pair of counter-rotating toroidal vortices in the cross-stream plane[1]. For Re > 22,200, the flow was unsteady periodic, and the symmetry of the motion of the flow about the mid-plane was broken by alternating periodic crossings of the toroidal vortices. Three-dimensional numerical simulations at Re = 22,200 and 44,400 further revealed that the toroidal vortices acquire a time-varying sinuous shape in the circumferential direction, and that the rigid-body rotation region contained very weak secondary motions.

The flow field between co-rotating disks is dramatically altered by the insertion of an arm between the disks to simulate the E-block arms of the HSA. The effects of radially-oriented obstructions between co-rotating disks was studied by several researchers including Lennemann [1], Tzeng and Humphrey [4], Usry *et al.* [6], Gor *et al.*

[1] The Reynolds number in [5] was based on the disk radius and the tip speed of the disks.

[7], Abrahamson *et al.* [8], and Suzuki and Humphrey [9]. Tzeng and Humphrey [4] and Usry *et al.* [8] used LDA to investigate the effects of relatively thin obstructions, with an obstruction thickness, *t*, to disk-to-disk spacing, *H*, ratios of $t/H = 0.25$ and $t/H = 0.21$, and blockage factors[2] β in the range of $7\% \leq \beta \leq 16\%$. They presented radial and axial mean and rms circumferential velocity profiles of the flow between the disks in the presence of the obstruction. Gor *et al.* [7] used LDA to investigate thicker arms, with $\beta = 23\%$ and $\beta = 46\%$. Abrahamson *et al.* [8] used a dye-injection flow visualization technique to investigate the effects of a relatively large obstruction, with $t/H = 0.57$, and $\beta = 60\%$. Suzuki and Humphrey [9] used numerical simulations to investigate the effects of relatively large obstructions, with $t/H = 0.67$, and $\beta = 31\%$ or $\beta = 62\%$. The simulations were carried out for a single obstruction, as well as for two obstructions simultaneously present in the space between the disks.

Recent disk drives employ a rotary HSA configuration where the sliders are in-line with the suspensions and arms, and the HSA follows a circular arc to position the head on the disk surface. Flow visualizations for the in-line rotary configuration drive were carried out by Girard *et al.* [10], who observed vortex shedding around the E-block arm tip, which originated from the flow along the leading edge and the trailing edge of the arm.

[2] The blockage factor for a radially-inserted obstruction was defined as $\beta = [tL]/[H(a+R-R_1)]$, where L is the length of the obstruction, a is the spacing between the disk tip and the shroud, R is the disk radius, and R_1 is the hub radius.

Early research on the effects of airflow in hard disk drives on suspension vibration was carried out by Yamaguchi *et al*. [11], where it was demonstrated that the amplitude of suspension vibration was proportional to the square of the approaching velocity. In subsequent research by Yamaguchi *et al*. [12, 13], the flow around a suspension was measured using hot-wire anemometry to identify the sources of suspension vibration, and numerical simulations of the flow were performed. It was shown in [12, 13] that suspension vibration was caused by the turbulence behind the suspension, and that employing an aerofoil shape for the suspension cross-section can reduce suspension vibration.

Gross *et al*. [14] investigated the effects of E-block arm thickness on head vibration in the off-track direction in a modeled HDD. Four E-block arms of thicknesses *1.0 mm*, *1.2 mm*, *1.4 mm*, and *1.6 mm* were tested at three radial positions: the inner diameter (ID), the middle diameter (MD), and the outer diameter (OD). The rms amplitudes of the off-track vibration were evaluated over the *0-20 kHz* range, and were broken down into components over the *0-2 kHz* and *2-20 kHz* frequency bands in order to assess the contributions of the structural resonances to the overall head off-track vibration. The *2-20 kHz* component was further divided into subcomponents over three frequency bands in order to evaluate the contributions of the E-block arm dynamics and the of the suspension dynamics to the overall vibration. The measured off-track rms amplitudes were dependent on the E-block arm thickness, and, for all radial positions, increased as the arm thickness was increased. This trend was also observed in the *0-2 kHz* component amplitudes. The *2-20 kHz* component amplitudes, however, did not follow

this trend. The *1.2 mm* arm resulted in the highest value for this component, and the *1.6 mm* arm resulted in the lowest. The trend assumed by the *2-20 kHz* component was strongly shaped by the component of off-track vibration resulting from the E-block arm dynamics.

In a subsequent study, Gross et al. [15] investigated the effects of E-block arm thickness on the airflow past the HSA in the same modeled drive tested in [14], primarily with the objective of shedding some light on the head vibration results presented in [14], especially the unexpected trend observed in the *2-20 kHz* component. Airflow measurements were taken using a constant temperature hot-wire anemometer, with and without the head gimbal assemblies (HGA's) attached to the arms, at the ID, the MD, and the OD positions. A correlation was observed at the ID position between the trend followed by the rms flow fluctuations in the region downstream of the E-block arms and that followed by the 2-20 kHz component of the vibration rms amplitudes presented in [14].

In this study, the effects of E-block arm thickness on airflow were investigated in the same modeled drive that was tested by Gross *et al.* in [14] and [15]. The same E-block arms, of thicknesses 1.0 mm, 1.2 mm, 1.4 mm, and 1.6 mm, were used. Airflow measurements were taken in the region downstream of the E-block arm using a constant-temperature hot-wire anemometer at the ID position. These flow measurements were conducted primarily with the goal of shedding some light on the head vibration results presented in [14], especially the unexpected trend observed in the 2-20 kHz component.

The specific objectives of this study were to form a better understanding of the local flow structure in the region downstream of the HSA, to observe the effects of E-block arm thickness on the flow characteristics in this region, and to gain insight into how the flow affects head vibration. In addition, the measurements obtained in this investigation may be taken as an experimental reference for the testing, development, and validation of numerical simulation procedures that aim at predicting the flow in HDD's.

2. Experimental Setup

2.1. Modeled Hard Disk Drive

The modeled drive that was used by Gross *et al.* [14, 15] was used for this study. The setup (see Fig. 1) was described in detail in [14]. Photographs of the HSA and the HGA used are presented in Figs. 2 and 3, respectively. The drive was operated at *10,000 rpm* (ω *= 1,047.2 rad/s*), the disk radius R was *42 mm*, the disk thickness *1.0 mm*, and the disk spacing *2.0 mm*. The four E-block arms tested[3] were of thicknesses *1.0 mm*, *1.2 mm*, *1.4 mm* and *1.6 mm*. These arms will henceforth be referred to as t10, t12, t14 and t16, respectively. The arm tip thickness at the swage area was *0.95 mm* for all arms. Figure 4 is a schematic of the setup that highlights the most relevant dimensions. The blockage factors[4] associated with the four E-block arms at the ID position are listed in Table 1.

[3] The E-block arms are the same ones used in [14] and [15].
[4] These blockage factors were based on the projected area of the arm leading edge on a radial plane.

2.2. Hot-Wire Anemometry

A customized constant-temperature hot-wire anemometer (TSI model 1276CF-10A) was used for measuring the flow field. The probe was the single sensor, capable of measuring flow speed amplitude, without providing any information about flow direction (Fig. 5). The body length of the anemometer probe was extended so that it could be inserted between the two disks. The probe diameter was *0.9 mm*, the sensor diameter *4 mm*, and the sensor length *0.2 mm*, which was *10%* of the disk-to-disk separation. The sensing wire was attached to the probe by two prongs that extended out *4 mm* from the end of the probe. The sensor was oriented with its axis parallel to the spin axis, and was centered between the two disks. It was therefore most sensitive to the in-plane flow velocity component at the mid-plane between the disks. The hot-wire probe body was nearly aligned with the expected mean flow direction to avoid vortex wrapping on the probe that would result in spurious contributions to the measurement. The output of the hot-wire anemometer was fed to an HP3563A signal analyzer. Software was written to perform the data acquisition and its initial processing. At each measurement point, the hot-wire anemometer output was averaged in the time domain to obtain the mean flow speed, $\hat{u}$. During this part of the measurement, the data rate was set low enough (frequency span of *1 kHz*, data record length of *800 ms*, *133* disk revolutions) to ensure that an accurate long-term mean flow speed was obtained. The dc component of the anemometer output was then removed and the data rate increased (frequency span of *20 kHz*, data record length of *40 ms*, *7* disk revolutions), and the output was averaged in the frequency domain to obtain an averaged power spectrum of the flow fluctuation, $\overline{G_{u'}(f)}$.

The fluctuation power spectra were used to calculate the rms flow fluctuation, u_{rms}, and its components according to Eq. (2).

The hot-wire anemometer was calibrated using a precision net flow apparatus prior to the measurements and its calibration curve was determined using least squares regression. A calibration reference measurement of the mean flow speed was taken immediately after calibration in the unobstructed flow between the disks. For each subsequent measurement set a reference measurement was taken at the same location as that of the calibration reference, so that a correction factor could be computed for the measurement set to account for ambient temperature variations.

All the measurements taken in this study were carried out at the ID position. For each arm the flow speed was measured in the region downstream of the arm tip, with no HGA's attached. The measurement region, shown to scale with the E-block arm in Fig. 6, was covered by scanning eight lines perpendicular to the arm trailing edge. These lines were located at distances $x = 2, 3, 4, 5, 6, 8, 10,$ *and 12 mm* away from the arm tip. The number and density of the measurement points along each line were determined during the measurement for each arm by starting with a course point-to-point step of *1.0 mm*, and then refining the step size with additional points to capture any steep gradients and local extrema of the mean flow speed and the rms fluctuation profiles along the line. Steps as small as *0.05 mm* between points were sometimes necessary to capture all the desired details of the profiles. At each measurement point, the flow was allowed to settle for a minimum of *1,000* disk revolutions before recording the data.

A second computer program was prepared to further process the mean and fluctuation power spectra outputs of the anemometer for each measurement. The mean flow speed $\hat{u}$ and the rms flow fluctuation u_{rms} and its components over several frequency bands were obtained using the anemometer calibration curve. The turbulence intensity *TI*, the mean dynamic head $\bar{h}$, and the rms dynamic head fluctuation h_{rms} and its components were also computed. The discrete values of $\hat{u}$, u_{rms}, *TI*, $\bar{h}$, h_{rms}, and the components of u_{rms} and h_{rms} at the measurement points were then interpolated in the *x* and *y* directions to generate continuous distributions of these quantities over the entire measurement region.

2.3. Data Analysis

The flow speed, *u*, in turbulent flow analysis is commonly expressed as the sum of the mean and fluctuating components of the speed, $\hat{u}$ and u', respectively

$$u = \hat{u} + u' . \tag{1}$$

The rms flow fluctuation, u_{rms}, can be computed from the spectrum analyzer output of the power spectrum $\overline{G_{u'}(f)}$ of the flow fluctuation, where *f* denotes frequency, according to[5]

$$u_{rms} = \sqrt{a \sum_i \overline{G_{u'}(f)}}, \tag{2}$$

where *a* is a scale factor for the windowing function used in calculating the power spectra. A Hanning window was employed in this study, for which *a = 2/3*.

[5] Eq. (2) is based on Parseval's theorem, which states that for an aperiodic function *x(t)* whose Fourier transform is *X(w)*,

$$\int_{-\infty}^{\infty} x^2(t)dt = 2p \int_{-\infty}^{\infty} |X(w)|^2 dw$$

The rms flow fluctuation is usually expressed as a percentage of the local mean flow speed. This percentage is known as the turbulence intensity, *TI*, of the flow, and it was computed at each measurement point according to

$$TI = \frac{u_{rms}}{\bar{u}}. \tag{3}$$

The drag force, *D*, on a body can be expressed as

$$D = \int_A C_D q dA, \tag{4}$$

where C_D, *A*, and *q* denote the sectional drag coefficient, the projection of the area of the body onto the flow direction, and the dynamic pressure, respectively. The dynamic pressure, *q*, is given by

$$q = \frac{1}{2} \rho u^2, \tag{5}$$

where ρ denotes air density and *u* denotes flow speed.

Substituting Eq. (1) into Eq. (5), we may express *q* as

$$\begin{aligned} q &= \frac{1}{2} \rho \left(\bar{u} + u'\right)^2 \\ &= \frac{1}{2} \rho \left(\left(\bar{u}\right)^2 + 2\bar{u}u' + \left(u'\right)^2 \right) \end{aligned} \tag{6}$$

Similar to velocity, dynamic pressure can be expressed in terms of its mean and fluctuating components, $\bar{q}$ and *q'*, respectively, as

$$q = \bar{q} + q'. \tag{7}$$

It follows from Eqs. (5) through (7) that

$$\bar{q} = \tfrac{1}{2}\rho\left(\left(\bar{u}\right)^2 + \overline{\left(u'\right)^2}\right), \tag{8}$$

and

$$q' = \tfrac{1}{2}\rho\left(2\bar{u}u' + \left(u'\right)^2 - \overline{\left(u'\right)^2}\right). \tag{9}$$

If $\hat{u}$ is much greater than $|u'|$, $\bar{q}$ will be dominated by the first term in the brackets of Eq. (8), and q' will be dominated by the first term in the brackets of Eq. (9), and they may be expressed approximately as

$$\bar{q} \approx \tfrac{1}{2}\rho\left(\bar{u}\right)^2, \tag{10}$$

and

$$q' \approx \rho\bar{u}u'. \tag{11}$$

The rms dynamic pressure fluctuation q_{rms} can now be written as

$$q_{rms} \approx \rho\bar{u}u_{rms}. \tag{12}$$

Consequently, the mean drag force $\overline{D}$ and the rms drag force D_{rms} can be approximated as

$$\overline{D} \approx \tfrac{1}{2}\int_A C_D\,\rho\left(\bar{u}\right)^2 dA, \tag{13}$$

and

$$D_{rms} \approx \int_A C_D\,\rho\bar{u}u_{rms}\,dA. \tag{14}$$

It is clear from Eqs. (8) and (9) that a higher rms flow fluctuation translates directly into a higher average drag force $\overline{D}$, and a higher rms drag force fluctuation D_{rms}. Eq. (14) also highlights the relevance of the quantity $\hat{u}u_{rms}$, since D_{rms} is approximately proportional to $\hat{u}u_{rms}$. Kim *et al.* [16] showed, through experimental investigation, a correlation between HGA vibration and $\hat{u}u_{rms}$.

The quantities $\overline{h}$ and h_{rms}, defined by,

$$\overline{h} = \frac{1}{2}\left(\left(\overline{u}\right)^2 + \left(u_{rms}\right)^2 \right) \approx \frac{1}{2}\left(\overline{u}\right)^2 \tag{15}$$

and

$$h_{rms} \approx \overline{u}u_{rms} . \tag{16}$$

will henceforth be loosely referred to as the mean dynamic head and the rms dynamic head fluctuations[6], respectively.

The disk surface speed V_d is given by

$$V_d = \omega r , \tag{17}$$

where ω is the disk angular speed.

[6] Strictly speaking, these quantities should be divided by the gravitational constant $g = 9.81\ m/s^2$ to yield the mean and rms dynamic head.

3. Experimental Results and Discussion

3.1. A Note on the Usefulness of the Airflow Results

Before proceeding with a presentation and discussion of the results, a note should be made about the extent of usefulness of the results. Figure 7(a) is a schematic that illustrates key axial dimensions[7] in the space between the two disks. The arm thickness shown is *1.2 mm*, and is the only dimension that varies for the different arms. It was noted earlier that the length of the sensing wire was *0.2 mm*, which was *10%* of the disk-to-disk spacing, *21%* of the arm tip thickness, and *13%*, *14%*, *17%*, and *20%* of the thicknesses of t16, t14, t12, and t10, respectively. Consequently, the mean and rms output values obtained at each measurement point, and the computed values of $\hat{u}$, u_{rms}, TI, $\overline{h}$, h_{rms}, and the components of u_{rms} and h_{rms}, represent spatial averages of these quantities over the length of the sensing wire, which is a fraction of the arm thickness. This increases the usefulness of the results because the dynamic pressure head distributions obtained (both mean and rms) provide information about average incremental drag forces $DD = C_D q(DA)$, as opposed to differential drag forces $dD = C_D q(dA)$, that would be generated on a body in the flow. This renders the computed distributions more representative of the drag forces experienced by the arms, and the HGA's, had they been in the flow.

The mean and rms flow speed profiles depicted in Figs. 7(b) and 7(c) are representative of some of the axial profiles expected between the two disks. Profiles

[7] Axial dimensions are shown to scale.

$\hat{u}_1(z)$, $\hat{u}_2(z)$, $u'_1(z)$ and $u'_2(z)$ are representative of the mean and rms circumferential velocity axial profiles measured in the obstructed flow between two co-rotating disks by Usry *et al.* [6] at of $r/R = 0.71$ and $r/R = 0.78$, 20^o downstream of the obstruction. Profiles $\hat{u}_2(z)$ and $u'_2(z)$ are representative of the mean and rms flow speed profiles presented in [6] at $r/R = 0.71$ and $r/R = 0.78$, 90^o downstream of the obstruction. Profiles $\hat{u}_2(z)$ and $u'_3(z)$ are representative of those measured for the unobstructed flow between two co-rotating disks by Schuler *et al.* [3] at $r/R = 0.714$ and $r/R = 0.781$, and Tzeng and Humphrey [4] at a $r/R = 0.726$, and are likely to be quite similar to the flow in the inner region more than 90^o downstream of the E-block arm tip. The latter remark is based on the reportings in [4, 6, 7, 8, 9] that the fluid motion rapidly recovers the mean characteristics of an unobstructed flow as the flow travels further downstream of the obstruction. Profiles $\hat{u}_3(z)$ and $u'_3(z)$ are expected to be representative of the flow passing between the arm tip and the rotating hub, where the flow speed exceeds that of the disk surface on account of the increased flow rate through that region as the flow approaching the arm is partially blocked and redirected towards the hub. The profiles above exhibit the common feature that they are nearly uniform around the mid-plane over the length of the arm. This is a feature that will be used to justify speculations made below.

At this stage, we will surmise that the flow in the space between the two disks at the measurement region is symmetric with respect to the mid-plane, and possesses mean and rms flow speed profiles similar to those presented in Figs. 7(b) and 7(c). Taking this assumption into consideration, along with the note above on the sensor length, it is reasonable to extend the comparison of the dynamic head distributions in the

measurement region to formulate conclusions, merely comparative in nature, about drag forces that would arise due to the complete dynamic pressure fields downstream of the arms.

4.2. Flow Characteristics

Figures 8 through 12 present the mean flow speed, rms flow fluctuation, turbulence intensity, mean dynamic head, and rms dynamic head fluctuation profiles, respectively, along the measurement lines at $x = 2, 4, 6, 8, 10,$ *and 12 mm* for t10. It should be noted that the mean flow speed profiles exhibit steep gradients, and that the rms fluctuation and turbulence intensity profiles exhibit peaks that coincide with the steep gradients in the mean speed. These features are characteristic of a classical shear layer observed in free turbulent flows [17]. The profiles for t12, t14, and t16, shown in Figs. 13 through 23, exhibit similar features, alluding to the existence of a shear layer in the flow. Further discussion of the flow characteristics and comparison of the flow around the four arms are deferred until after the distributions of $\hat{u}$, u_{rms}, TI, $\overline{h}$, h_{rms}, and the components of u_{rms} and h_{rms} are presented.

In spite of their relevance in detailing out the flow characteristic profiles, the results as presented in Figs. 8 through 23 are difficult to assimilate, and do not readily lend themselves to the task of comparing the flow fields downstream of the four arms. In order to make the results easier to interpret and to provide a more coherent account of the flow characteristic fields in the measurement region, we interpolated the data in the x and

y directions (indicated in Fig. 6) and generated distributions of the flow characteristics over the entire region.

Figure 28 depicts two color contour plots of the disk surface speed, generated using two color scales. The plot in Fig. 28(a) employs the first scale, which is an automatic scale showing the full range of the disk circumferential velocity. The plot in Fig. 28(b) employs a clipped color scale that is used in all subsequent mean flow speed distribution plots to allow for comparison with the results for the different cases considered. The upper limit in the latter scale is based on the maximum mean flow speed measured with the E-block arms inserted between the disks. These figures are very similar to the schematic of Fig. 6, with the arm and measurement region rotated slightly to align the *x*-axis with the horizontal. An outline of the E-block arm tip is shown as solid lines, and an outline of the HGA is shown as dashed lines. The HGA component outlines are labeled in the figure. It should be emphasized that the flow measurements were conducted with no HGA's attached to the E-block arm, and that the HGA outlines are included in these figures, and in subsequent ones, merely for reference. Due to space limitations, the arm tip outline will be omitted, and only the portion of the HGA outline within the measurement region will be illustrated in the figures that follow.

The mean flow speed distributions for t10, t12, t14, and t16 are presented in Fig. 29. The distributions were generated using different scales, precluding quantitative comparison across the plots, and have been included for a qualitative comparison of the expected main flow direction, especially in the area that would be occupied by the HGA.

The plots for all arms demonstrate a high flow speed region along the upper edge of the HGA outline, with a steep gradient region immediately below it over which the mean speed drops to noticeably lower levels. Although no direct evidence of the flow direction has been obtained in this investigation, speculations about the flow direction are justified, based on flow visualization results presented by Girard *et al.* [10] in a similar geometric setup, and on the characteristics of the shear layer alluded to earlier. The approximate main flow direction can be inferred from the plots by following the locus of the maximum mean flow speed across the measurement lines, which is indicated by the dark red area. This exercise suggests the flow crosses the HGA's at a greater angle as the arm thickness decreases, which implies a greater projection of the area of the HGA onto the flow direction. Such an observation can be explained by noting that as the arm thickness increases, more of the flow upstream of the arm is blocked by the arm and redirected with greater speed towards the hub. In fact, the plot for t16 suggests that most of the main flow overshot the HGA. The relevance of this remark stems from the direct proportionality of the mean and rms drag forces to the projected area of the body onto the flow direction, expressed in Eqs. (13) and (14). It should be noted that some areas of the contours appear jagged due to the interpolation of sparse data, since the measurement grid was coarser in the horizontal direction than the vertical direction, as shown in Fig. 6.

The mean flow speed fields in the measurement region for t10, t12, t14, and t16 were regenerated using *the same scale* for all arms, and are presented in Fig. 30. For all arms there is a high mean flow speed zone along the upper edge of the HGA outline, and a low mean flow speed zone below that, with a steep speed gradient in between. This

distribution is attributed to the presence of the arm, as it partially blocks the upstream flow and redirects it towards the gap between the hub and the arm tip. A comparison of Figs. 28(b) and 30 reveals that the flow speed is much lower than the disk surface speed over most of the measurement region, and that, for t14 and t16, the local speed of air exceeds that of the disk surface around the upper edge of the tip of the HGA outline, as the air accelerates through the gap between the arm tip and the rotating hub. A comparison of the plots of Fig. 30 indicates that increasing the arm thickness resulted in elevating the mean flow speed in the entire measurement region. The HGA outline exhibited higher flow speeds for t12 than it did for t10, primarily due to the increase in the overall mean flow speed. The HGA outline exhibited slightly higher flow speeds for t14 than it did for t12, especially near the top edge of the slider. For t16, although the measurement region experienced the higher flow speed level, most of the high-speed flow overshot the HGA outline, and the outline seems to be subject to a similar level of flow speed to that of t10, if not lower. The significance of this trend follows from the following two points: the mean drag force on the HGA is proportional to the square of the approaching flow speed, as expressed in Eq. (13); and the rms drag force fluctuation acting on the HGA is directly proportional to the approaching flow speed, as shown in Eq. (14).

The mean dynamic head color contour plots are shown in Fig. 31. These distributions follow the same trend as that observed for the mean flow speed distributions: a result which is expected due to the approximation given in Eq. (10).

Figure 32 presents the rms flow fluctuation distributions for t10, t12, t14, and t16. The plots immediately reflect the increase in the level of flow fluctuation as the arm thickness was increased. The high-fluctuation region in these plots begins near the upper edge of the HGA outline, and coincides with the steep gradient in the mean flow speed distributions. As noted earlier, this feature is characteristic of a classical shear layer observed in free turbulent flows, and supports the assertion earlier about the flow direction, since in a classical shear layer the high-fluctuation region closely follows the main flow on the higher-speed side of the layer. The high-fluctuation area of t16 does not extend to the tip of the HGA as it does for the other three arms. A small additional area with relatively high fluctuation appears near the upper edge of the tip of the HGA outline (around $x=12$, $y=3$) in the t16 distribution. It should be noted that the high-fluctuation regions appear to be scattered in these plots due to the interpolation of sparse data, since the measurement grid is coarser in the horizontal direction than the vertical direction.

The turbulence intensity and the rms dynamic head fluctuation distributions of the four arms are shown in Figs. 33 and 34, respectively. The plots of Fig. 34 clearly reveal an increase in the rms dynamic head fluctuation level, both in the measurement region and within the HGA outline, as the arm thickness was increased from t10 to t12 to t14. The overall dynamic head fluctuation in most of the measurement region for t16 appears to be higher than that for t14, the exception being the area near the HGA tip. It is difficult to assess whether the HGA outline contains a higher overall level of dynamic head fluctuation in the t14 or the t16 cases. The high-fluctuation region in the t14 distribution

extends to the tip of the HGA, whereas the region in the t16 distribution attains the highest level of fluctuation, and spreads out more in the *y* direction.

In order to obtain more diagnostic information about the airflow excitation and its relation to the head off-track vibration, the rms flow fluctuation and the rms dynamic head fluctuation were decomposed into components over the frequency bands considered by Gross *et al.* [14]. Namely, the rms fluctuations were decomposed into components over the *0-2 kHz* and the *2-20 kHz* frequency bands. The contributions of the *0-2 kHz* components were noticeably greater than those of the *2-20 kHz* components. The *2-20 kHz* components were further divided into subcomponents over the *2-6 kHz*, the *6-10 kHz*, and the *10-20 kHz* frequency bands. The contributions of these components were highest for the *2-6 kHz* components, followed by the *6-10 kHz* components, followed by the *10-20 kHz* components.

Figures 35 and 36 depict the distributions of the *0-2 kHz* components of the rms flow fluctuation and the rms dynamic head fluctuation, respectively. The figures reveal that as the arm thickness was increased both of these components increased in the measurement region, and within the HGA outline as well, with the exception of the area around the HGA tip outline in t16. As was the case with the rms fluctuation, the high-fluctuation area of t16 of both components does not extend to the tip of the HGA as it does for t10, t12, and t14. The high-fluctuation areas in the t16 distributions spread to cover a wider portion (in the *y* direction) of the HGA around the baseplate than they do in the t14 distributions, and a small additional area with relatively high fluctuation appears

near the upper edge of the tip of the HGA outline (around *x=12*, *y=3*) in the t16 distribution. Thus, it is difficult to judge whether the HGA outline contains a higher overall level of fluctuation in the *0-2 kHz* band for the t14 or the t16 cases.

The *2-20 kHz* components of the rms flow fluctuation and the rms dynamic head fluctuation are presented in Figs. 37 and 38, respectively. An examination of these plots indicates that the levels of these components, especially within the HGA outline, increased as the arm thickness was increased from *1.0 mm* to *1.2 mm*, then they decreased as the thickness was increased to *1.4 mm*, and then decreased further as the thickness was increased to *1.6 mm*.

Figures 39 and 40 portray the *2-6 kHz* components of the rms flow fluctuation and the rms dynamic head fluctuation, respectively. These components appear to follow the same trend as that observed for the *2-20 kHz* components. The *6-10 kHz* components of the rms flow fluctuation and the rms dynamic head fluctuation are presented in Figs. 41 and 42, respectively. The overall levels of the flow fluctuation components appear to be highest for t12 and t14, followed by t10, and finally t16. The levels of this component of the dynamic head fluctuation within the HGA outline seem to be highest for t12, followed by 14 and t10, and finally t16. The *10-20 kHz* components of the rms flow fluctuation and the rms dynamic head fluctuation are presented in Figs. 43 and 44, respectively. It is difficult to compare the overall levels of the flow fluctuation components of Fig. 43. However, the levels of *10-20 kHz* components of the rms dynamic head fluctuation clearly follow the same trend as that observed in the *2-20 kHz*

frequency band: t12 appears to have the highest level of fluctuation, followed by t14 and t10, and finally t16.

Figure 45 depicts the power spectra of the hot-wire anemometer output at the measurement points along the line at $x = 2\ mm$ for the four arms. The plots are three-dimensional, with frequency on the horizontal axis, dB amplitude on the vertical axis, and y-position (along the $x = 2\ mm$ line) on the third axis. Each curve within a plot represents the power spectrum at a certain y-position along the measurement line, and the color contour has also been included to illustrate the magnitude of the power spectra. The plots for t10, t12, and t14 have been given the same view, with the origin on the right hand side and frequency increasing from right to left, whereas the plot for t16 has the origin on the left hand side, because these views best demonstrate the plot features described below. All power spectra exhibit a peak at 167 Hz, which coincides with the disk rotation speed, and is attributed to disk runout. The power spectra illustrate the dominance of the low frequency components; the high frequency energy is more pronounced only in the range of y = -6 to 0.5 mm. The plots also reveal the presence of clearly identifiable vortex shedding peaks in the power spectra. Two coherent vortex shedding peaks were observed in the power spectra of each arm along the $x = 2\ mm$ line. The frequencies of these peaks, f_v, are listed in Table 2. These are the frequencies in the separated region and the shear layer, and were generated by the flow separation from the arm.

For bodies with simpler geometries, the frequencies of the vortex shedding peaks can be correlated using the Strouhal number St defined by

$$St = \frac{f_v d}{U}, \tag{18}$$

where f_v, d, and U are the vortex shedding frequency (cycles/sec), the characteristic length of the body, and the characteristic speed of the approaching flow, respectively.

The Reynolds number *Re* is defined by

$$Re = \frac{Ud}{\nu}, \tag{19}$$

where ν is the kinematic viscosity of air. The values of *Re* for the four arms and the arm tip were computed using $U = 20$ *m/s*, $\nu = 1.512 \times 10^{-5}$ m^2/s, and d = arm thickness, and are listed in Table 2.

It is known from experimental results that the Strouhal number remains essentially constant at $St \approx 0.21$ for the free flow over a circular cylinder with a Reynolds number in the range $400 < Re < 10{,}000$ [17]. Since the Reynolds numbers listed in Table 2 are within the range above, a Strouhal number $St = 0.21$ may be used to estimate the vortex shedding frequencies $f_{cyl,t}$ for the free flow over a cylinder with $U = 20$ *m/s* and a characteristic diameter d set equal to *0.95 mm*, *1.0 mm*, *1.2 mm*, *1.4 mm*, and *1.6 mm*. The computed values of $f_{cyl,t}$ are listed in Table 2. Even though these estimates cannot be used to predict the vortex shedding frequencies for the E-block arms, a comparison of the f_v and $f_{cyl,t}$ columns of Table 2 indicates that they provide a reasonable approximation of the frequencies observed.

Figures 46 and 47 present the power spectra of the hot-wire anemometer output at measurement points along the lines at $x = 4$ *mm* and $x = 6$ *mm*, respectively. These figures show that the peaks were still identifiable on the *4 mm* line, but their amplitudes had diminished considerably. Along the *6 mm* line, the their amplitudes had diminished to the point where they could barely be identified from the spectra.

4.3. The Relationship Between Flow Fluctuation and Head Off-track Vibration

Plots of the total and component amplitudes of the rms head off-track vibration at the ID position measured by Gross *et al*. [14] are repeated, for convenience, in Figs. 48 through 53. Figure 48 shows that the rms head off-track vibration amplitudes increase as the arm thickness is increased, with only a slight difference between t12 and t14. This trend agrees with the trend followed by the rms flow fluctuation levels and the rms dynamic head fluctuation levels in the measurement region, depicted in Figs. 32 and 34, especially within the HGA outline.

Figure 49 demonstrates that the 0-2 kHz rms vibration component amplitudes increased as the arm thickness was increased. This trend correlates with the trends followed by the 0-2 kHz components of the rms flow fluctuation and the rms dynamic head fluctuation within the HGA outline, illustrated in Figs. 35 and 36.

Figures 50, 37, and 38 clearly indicate a good correlation between the trends followed by the 2-20 kHz rms components of the off-track vibration, the flow fluctuation, and the dynamic pressure fluctuation. The trend and the correlation observed in this

component carries over to the 6-10 kHz and the 10-20 kHz rms components of the off-track vibration, the flow fluctuation, and the dynamic pressure fluctuation.

4. Conclusion

The effects of E-block arm thickness on the flow in the region downstream of the arm tip at the ID position were investigated experimentally in a modeled HDD. The mean flow speed and the flow fluctuation power spectra were measured using a single-sensor hot-wire anemometer at the mid-plane between two disks, in the presence of an arm with no HGA's attached between the disks. The measurements were carried out for four arms, of thicknesses *1.0*, *1.2*, *1.4*, and *1.6 mm*, and were used to compute the mean and rms flow speed, the turbulence intensity, the mean and rms dynamic head, and the rms components of the flow fluctuation and the dynamic pressure fluctuation over the same frequency bands considered by Gross *et al.* [14] in their rms off-track vibration breakdown.

The rms dynamic head fluctuation breakdown revealed a good correlation between the rms dynamic pressure fluctuation components and the corresponding rms off-track vibration components over the same frequency bands. Specifically, a good correlation was observed between these components over the 0-20 kHz, 0-2 kHz, 2-20 kHz, 6-10 kHz, and 10-20 kHz frequency bands. The flow fluctuation power spectra

unveiled the presence of clearly identifiable vortex shedding peaks for all four arms. The vortex shedding frequencies corresponding to these peaks were identified.

5. Acknowledgements

This study was supported by the Computer Mechanics Laboratory at the University of California at Berkeley, the Hard Disk Drive Division at Fujitsu Ltd., and the Information Storage Industry Consortium.

6. References

[1] Lennemann, E., “Aerodynamic Aspects of Disk Flies”, IBM Journal of Research and Development, 1974, 18, pp. 480.

[2] Abrahamson, S. D., Eaton, J. K., and Koga, D. J., “The Flow Between Shrouded Corotating Disks,” Physics of Fluids A, 1989, Vol. 1, No. 2, pp. 241-251.

[3] Schuler, C. A., Usry, W., Webber, B., Humphrey, J. A. C., and Grief, R., “On the Flow in the Unobstructed Space Between Shrouded Corotating Disks,” Physics of Fluids A, 1990, Vol. 2, No. 10, pp. 1760-1770.

[4] Tzeng, H., and Humphrey, J. A. C., 1991, “Corotating Disk Flow in an Axisymmetric Enclosure With and Without a Bluff Body,” International Journal of Heat and Fluid Flow, Vol. 12, No. 3, pp. 194-201.

[5] Humphrey, J. A. C., Schuler, C. A., and Webster, D. R., 1995, “Unsteady Laminar Flow Between a Pair of Disks Corotating in a Fixed Cylindrical Enclosure,” Physics of Fluids, Vol. 7, pp. 1225-1240.

[6] Usry, W., Humphrey, J. A. C., and Grief, R., “Unsteady Flow in the Obstructed Space Between Disks Corotating in a Cylindrical Enclosure,” ASME Journal of Fluids Engineering, 1993, Vol. 115, pp. 620-626.

[7] Gor, D, Humphrey, J. A. C., and Grief, R., “Ventilated Flow Between Corotating Disks with Large Obstructions in a Fixed Cylindrical Enclosure,” ASME Journal of Fluids Engineering, 1994, Vol. 116, pp. 828-834.

[8] Abrahamson, S. D., Chiang, C., and Eaton, J. K., “Flow Structure in Head-Disk Assemblies and Implications for Design,” Advances in Information Storage Systems, 1991, Vol. 1, pp. 111-132.

[9] Suzuki, H., and Humphrey, J. A. C., “Flow Past Large Obstructions Between Co-Rotating Disks in Fixed Cylindrical Enclosures,” Journal of Fluids Engineering, 1997, Vol. 119, pp. 499-505.

[10] Girard, J., Abrahamson, S., and Uznanski, K., “The Effect of Rotary Arms on Co-Rotating Disk Flow,” ASME Journal of Fluids Engineering, 1995, Vol. 117, pp. 259-262.

[11] Yamaguchi, Y., Takahashi, K., Fujita, H. and Kuwahara, K., "Flow Induced Vibration of Magnetic Head Suspension in Hard Disk Drive", IEEE Transaction on Magnetics, Vol. 22, No. 5, September 1986, pp. 1022-1024.

[12] Yamaguchi, Y., Talukder, A.A., Shibuya, T. and Tokuyama, M., "Air Flow Around a Magnetic-Head-Slider Suspension and Its Effect on Slider Flying-Height

Fluctuation", IEEE Transaction of Magnetics, Vol. 26, No. 5, September 1990, pp. 2430-2432.

[13] Tokuyama, M., Yamaguchi, Y., Miyata, S. and Kato, C., "Numerical Analysis of Flying-Height Fluctuation and Positioning Error of Magnetic Head due to Flow Induced by Disk Rotation", IEEE Transaction of Magnetics, Vol. 27, No. 6, November 1991, pp. 5139-5141.

[14] Gross, H. M., Watanabe, T., and Bogy, D. B., "The Effects of E-Block Arm Thickness on Head Vibration Between Co-Rotating Disks in a Modeled Hard Disk Drive", CML Technical Report, No. 02-018, December 2002.

[15] Gross, H. M., Watanabe, T., Bogy, D. B., and Savas, Ö., "The Effects of E-Block Arm Thickness on the Airflow Past the Head Stack Assembly in a Modeled Hard Disk Drive", CML Technical Report, No. 02-019, December 2002.

[16] Kim, B.-C. and Mote, C.D., "Suppressing Turbulence Induced Vibration of the Head Suspension Assembly in a Hard Disk Drive", CML Technical Report, No. 99-015, August 1999.

[17] Schlichting, H., "Boundary-Layer Theory", McGraw-Hill, Inc., 7th Edition, 1979.

Arm	Thickness [mm]	Blockage Factor at ID
t10	1.0	27%
t12	1.2	31%
t14	1.4	36%
t16	1.6	40%

Table 1: Blockage factors for the E-block arms at the ID.

Arm	*Re*	f_v [kHz]	$f_{cyl,t}$ [kHz]
arm tip	1260	-	4.4
t10	1320	3.8, 4.5	4.2
t12	1590	2.6, 3.5	3.5
t14	1850	3.0, 3.8	3.0
t16	2120	2.8, 3.8	2.6

Table 2: Reynolds numbers and vortex shedding frequencies.

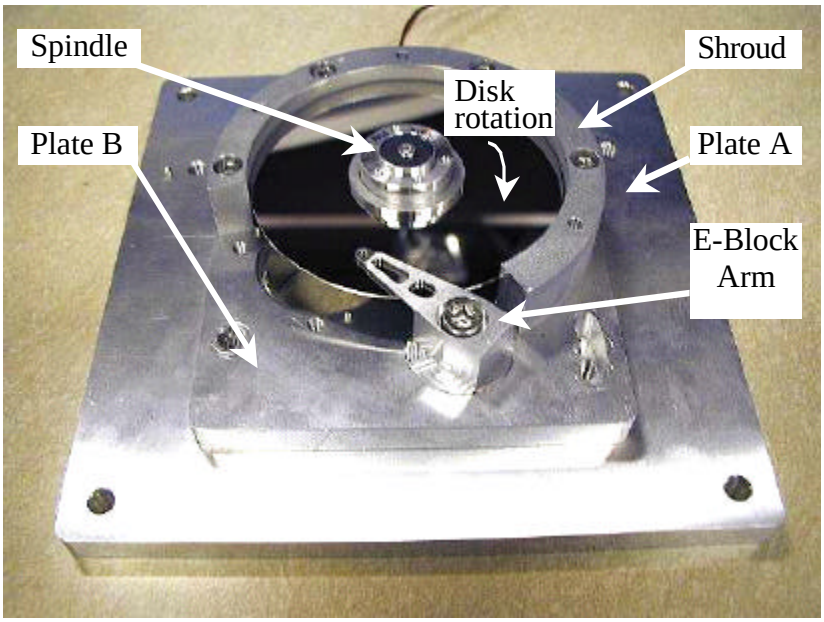

(a) Setup without top disk and cover

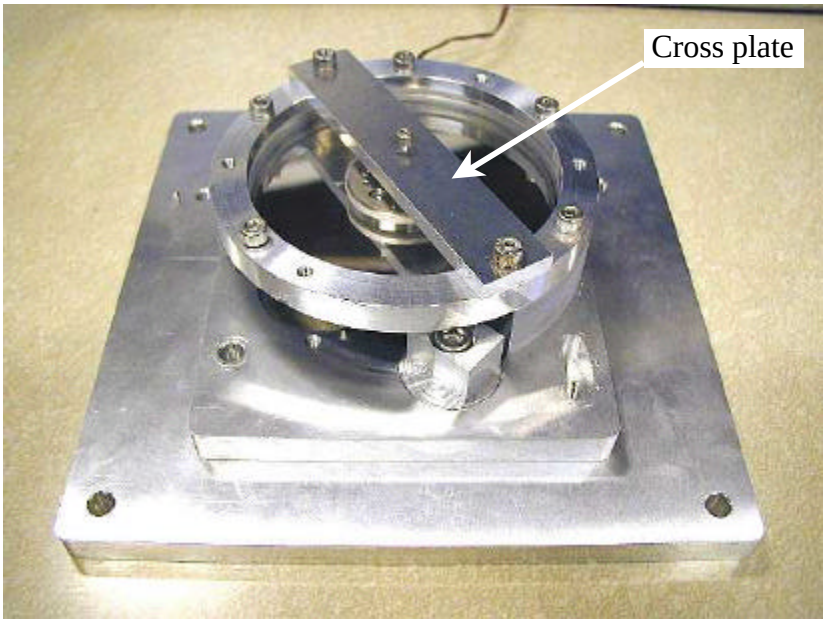

(b) Setup with top disk and cover
Figure 1: Modeled hard disk drive.

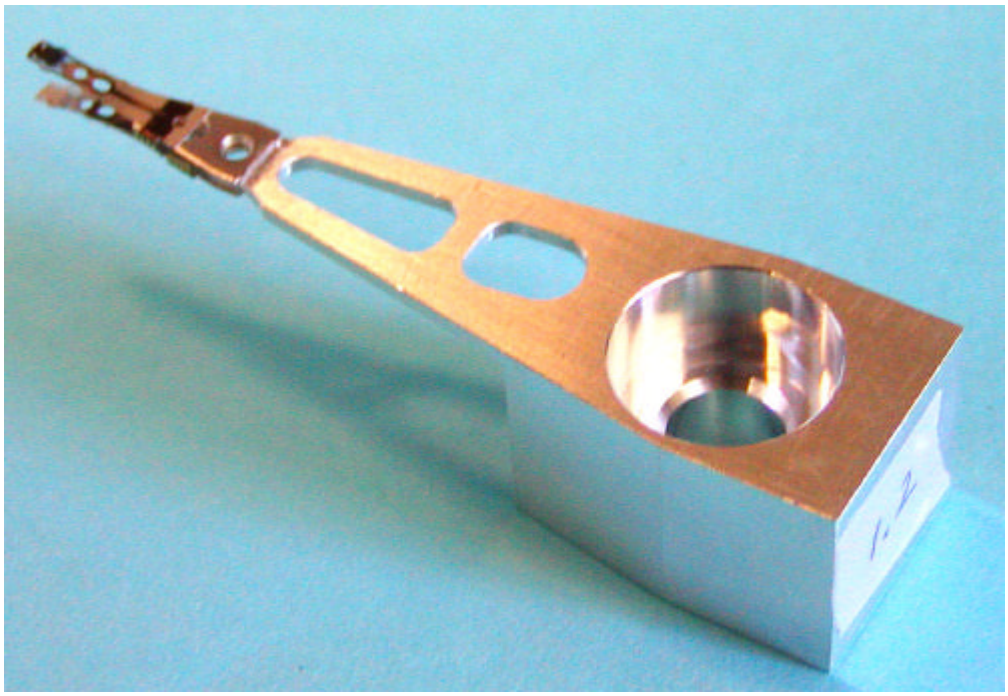

Figure 2: A close-up of the HSA.

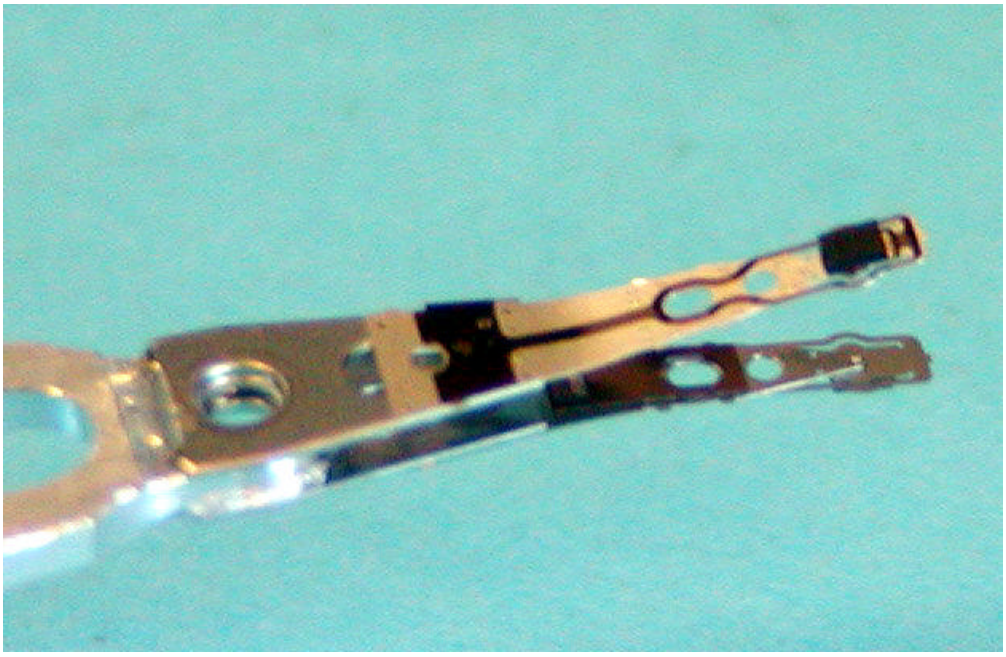

Figure 3: A close-up of the HGA.

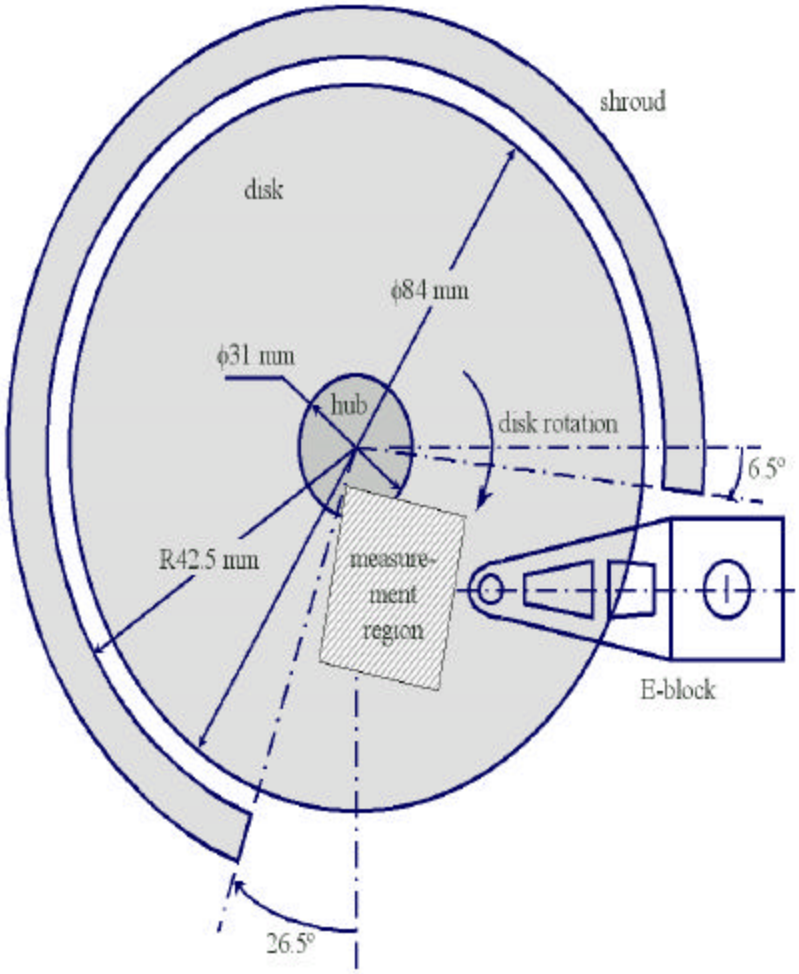

Figure 4: Schematic of the setup.

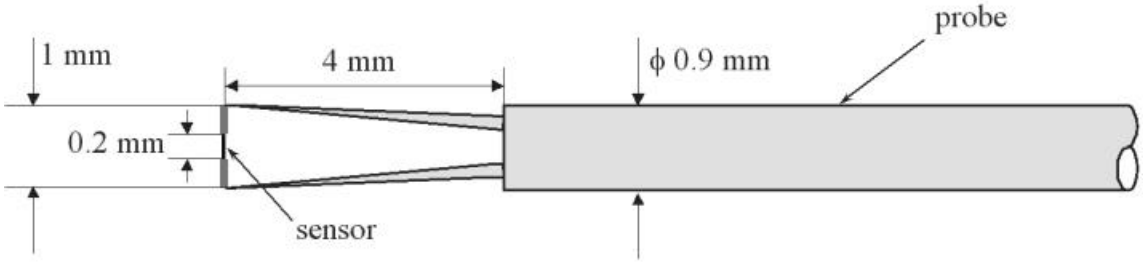

Figure 5: Schematic of the hot-wire probe.

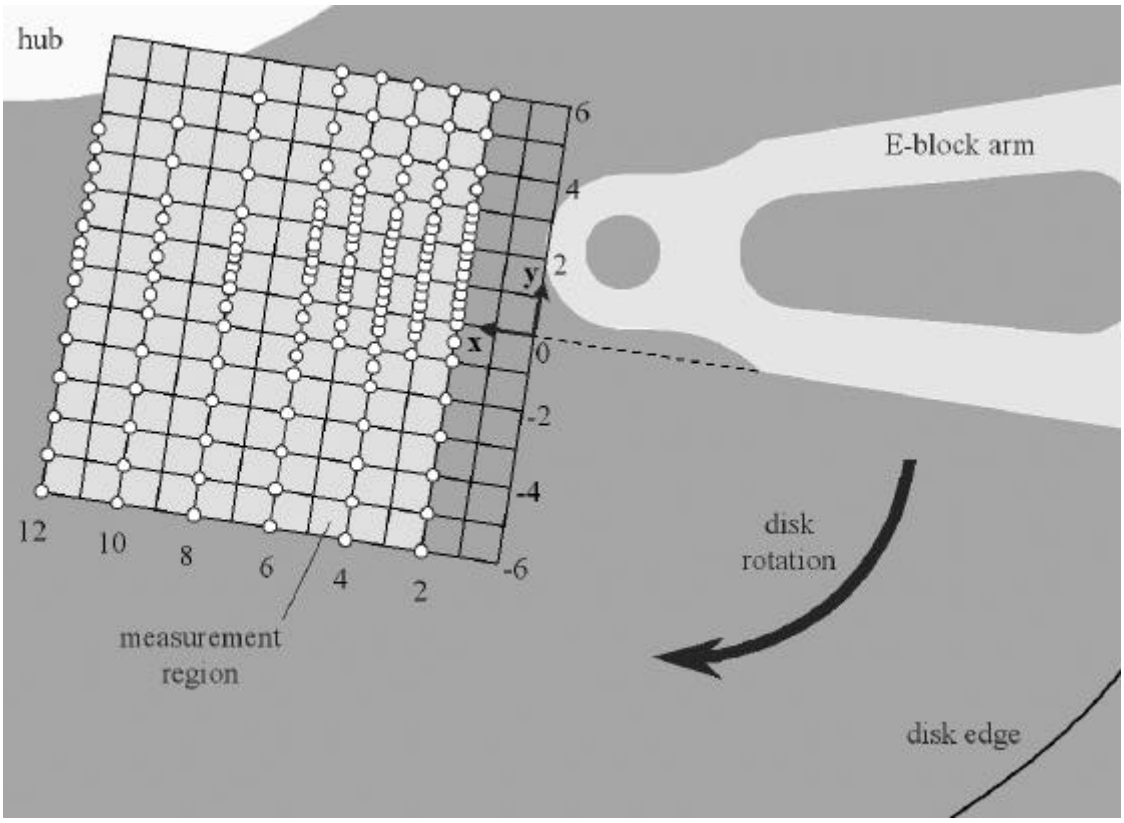

Figure 6: Airflow measurement region; measurement points marked by (o).

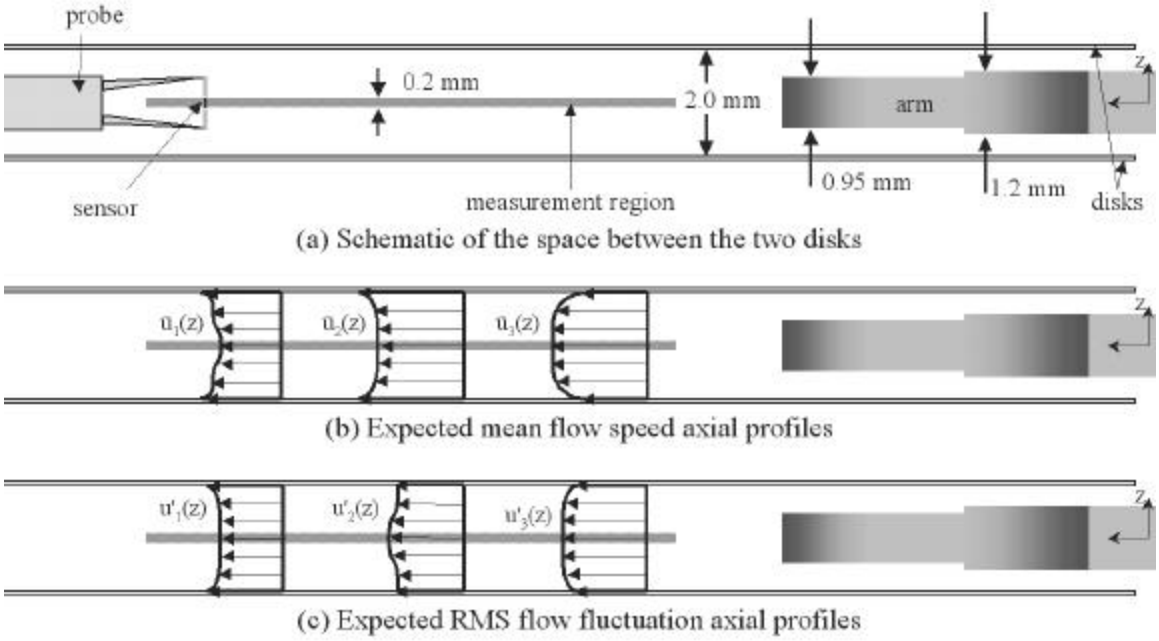

Figure 7: Schematic of space between the disks;
expected mean and RMS flow speed profiles.

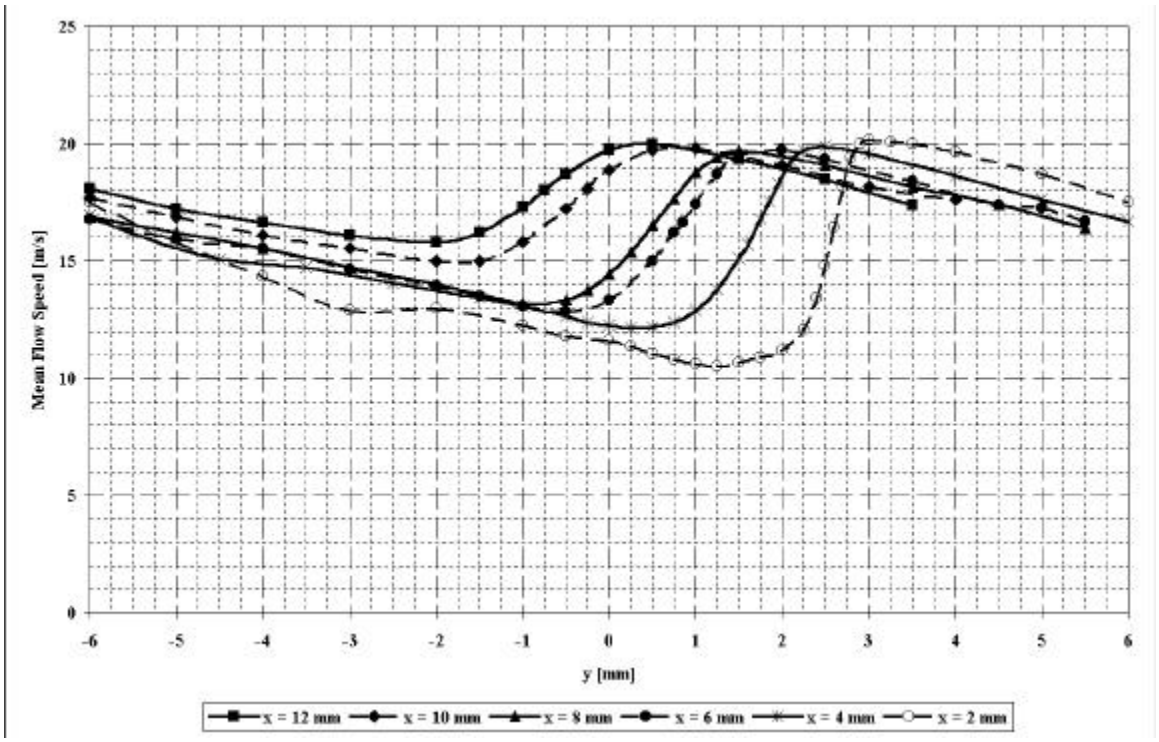

Figure 8: Mean flow speed profiles; t10.

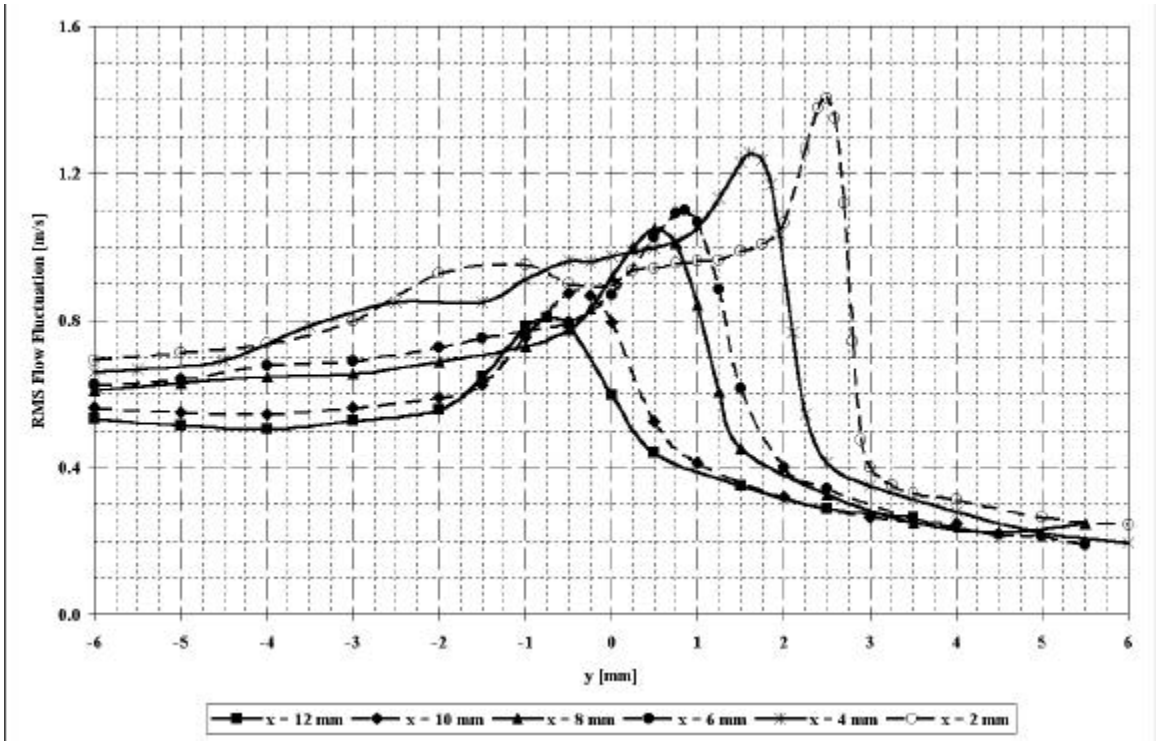

Figure 9: RMS flow fluctuation profiles; t10.

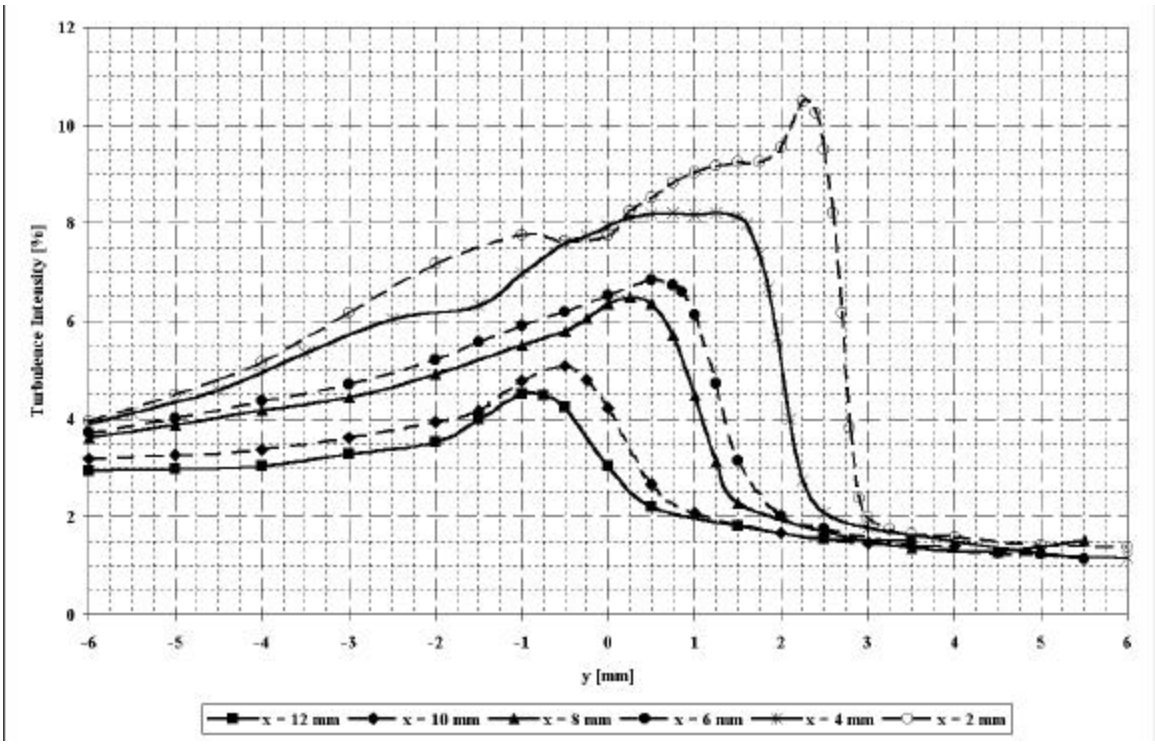

Figure 10: Turbulence intensity profiles; t10.

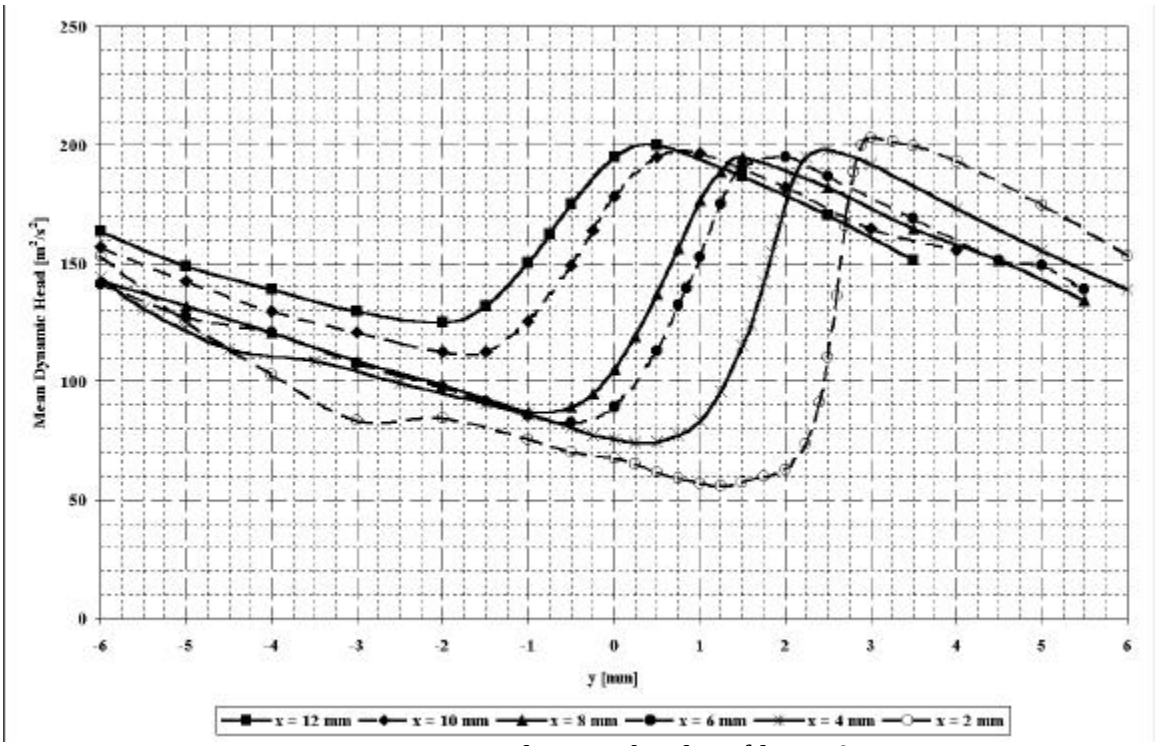

Figure 11: Mean dynamic head profiles; t10.

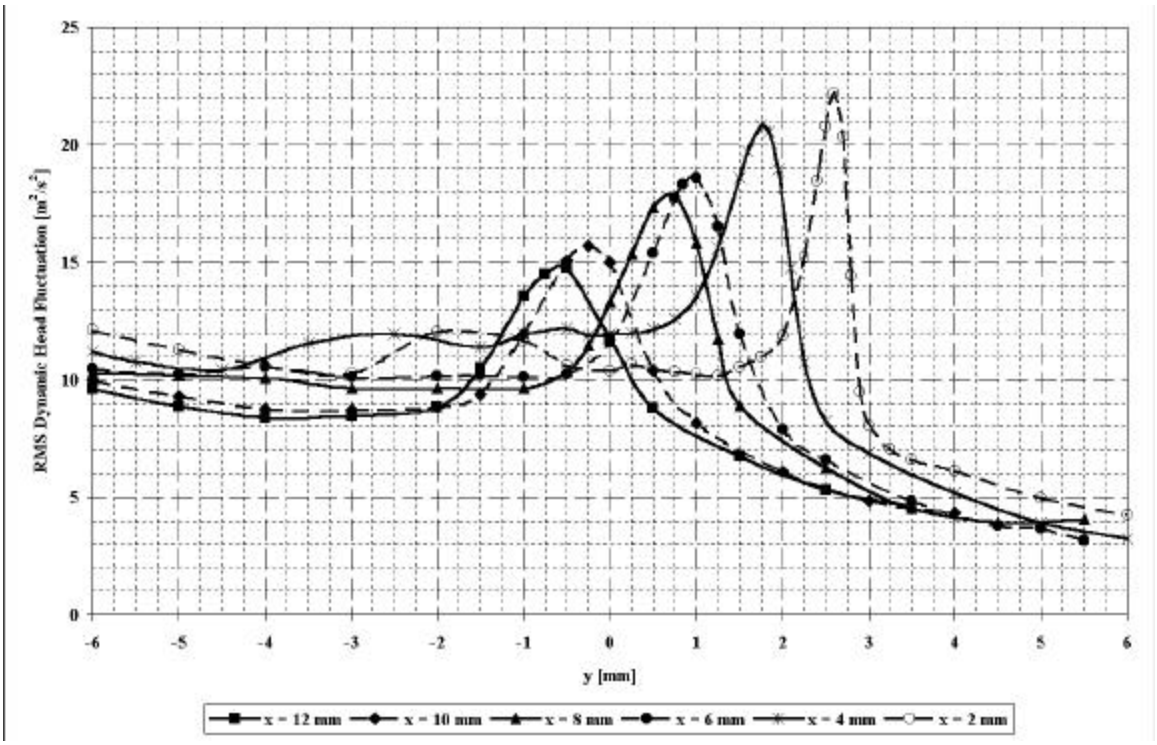

Figure 12: RMS dynamic head fluctuation profiles; t10.

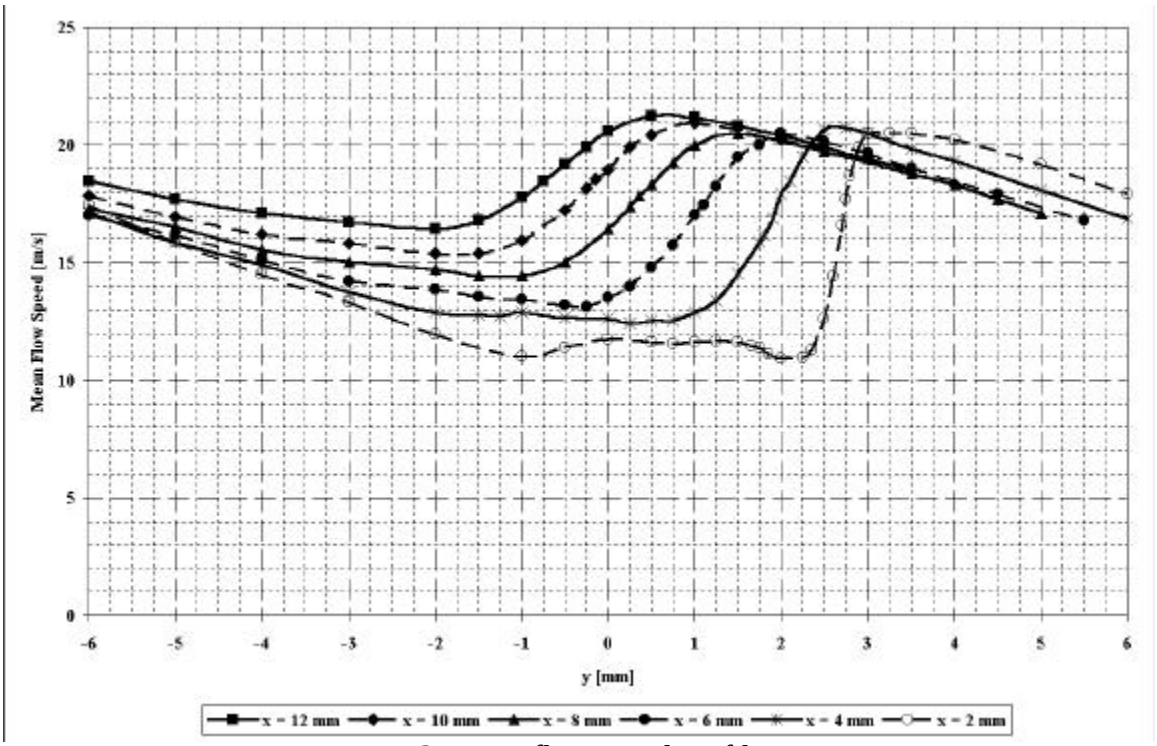

Figure 13: Mean flow speed profiles; t12.

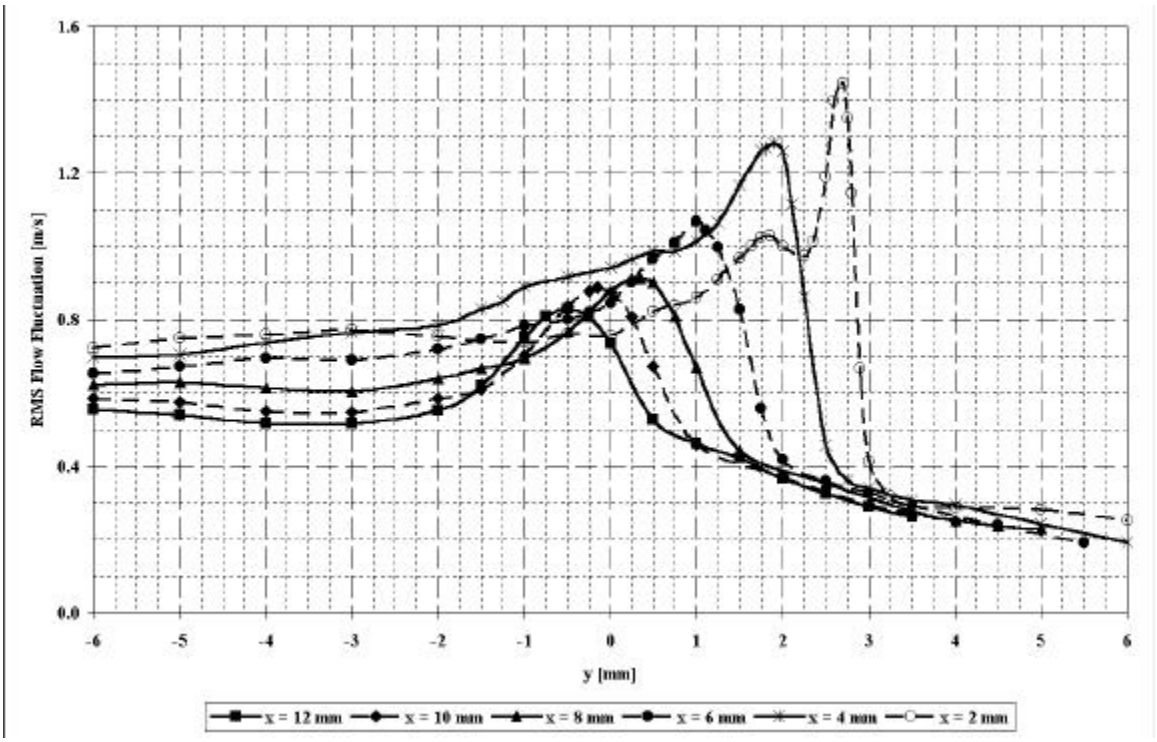

Figure 14: RMS flow fluctuation profiles; t12.

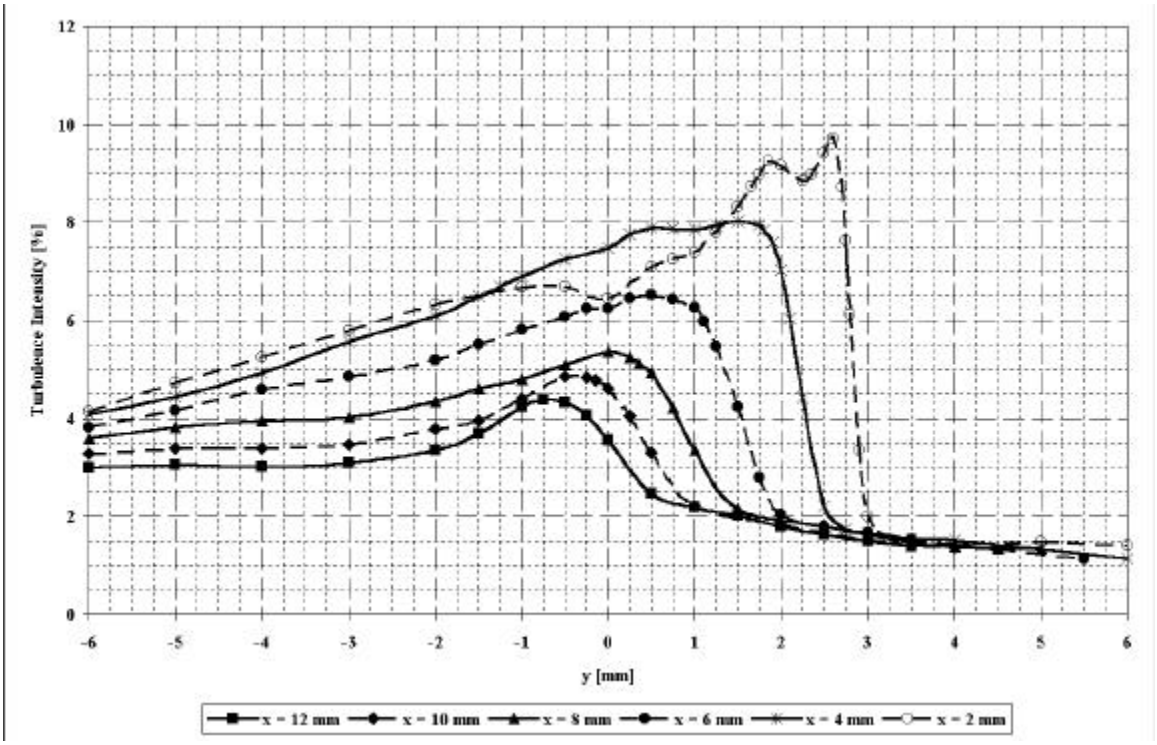

Figure 15: Turbulence intensity profiles; t12.

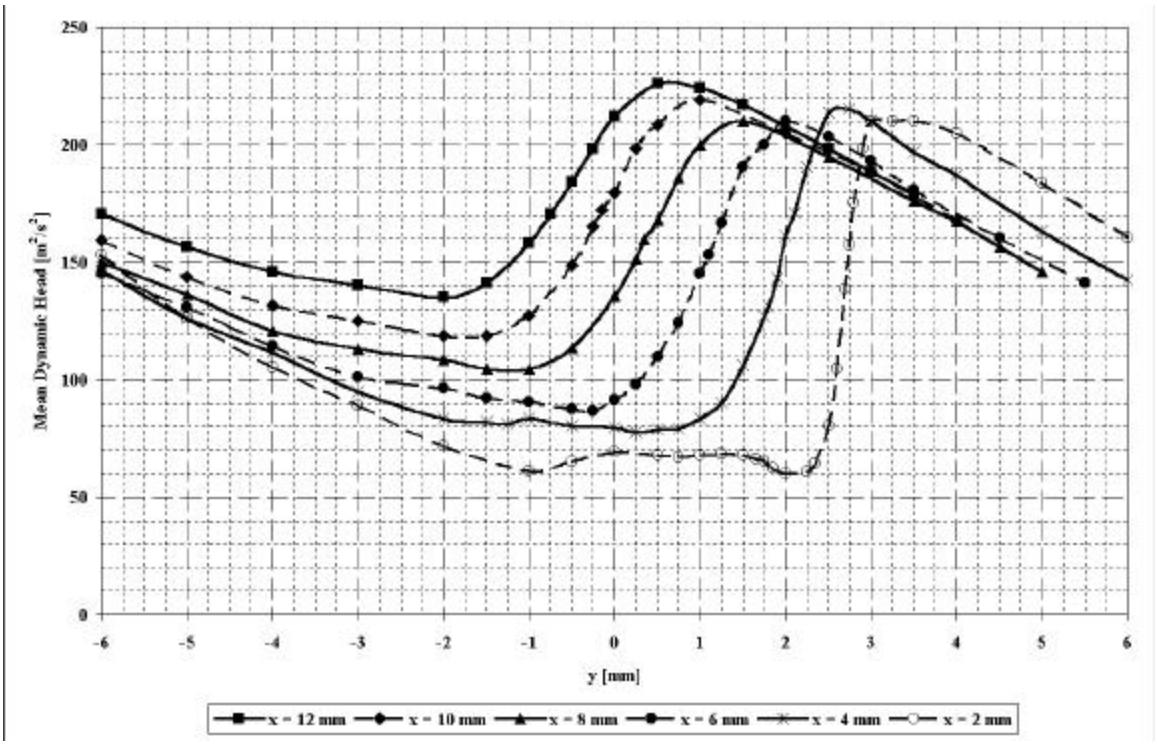

Figure 16: Mean dynamic head profiles; t12.

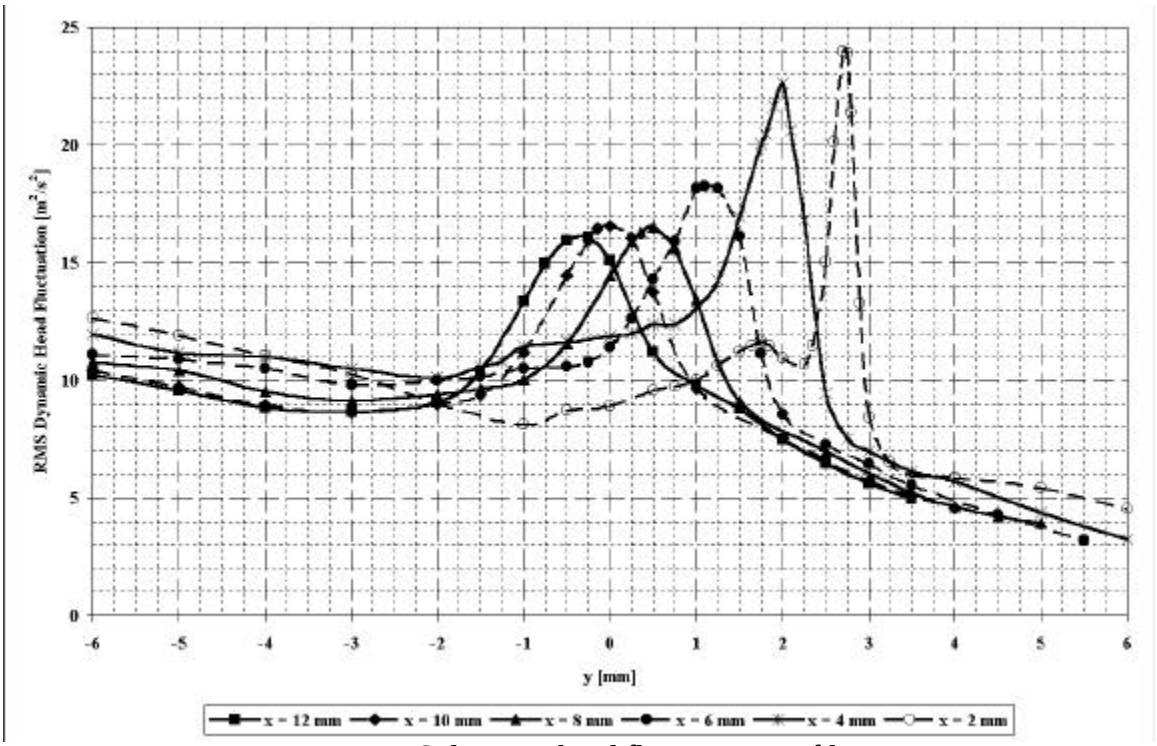

Figure 17: RMS dynamic head fluctuation profiles; t12.

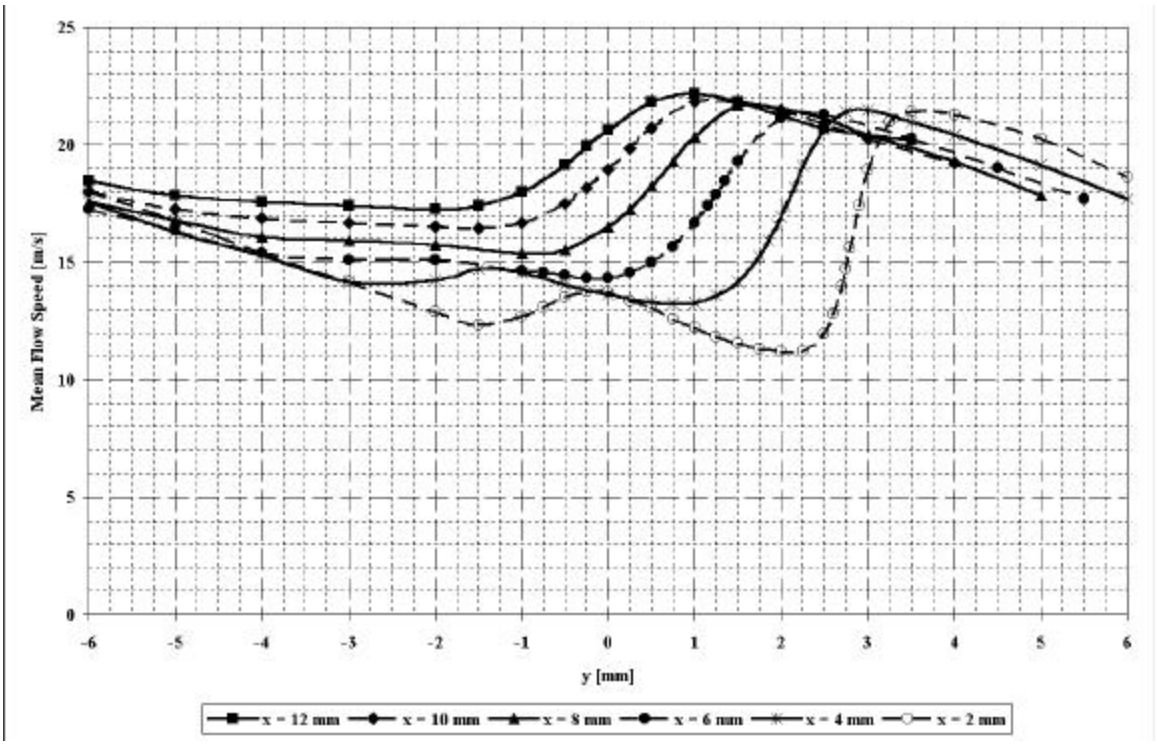

Figure 18: Mean flow speed profiles; t14.

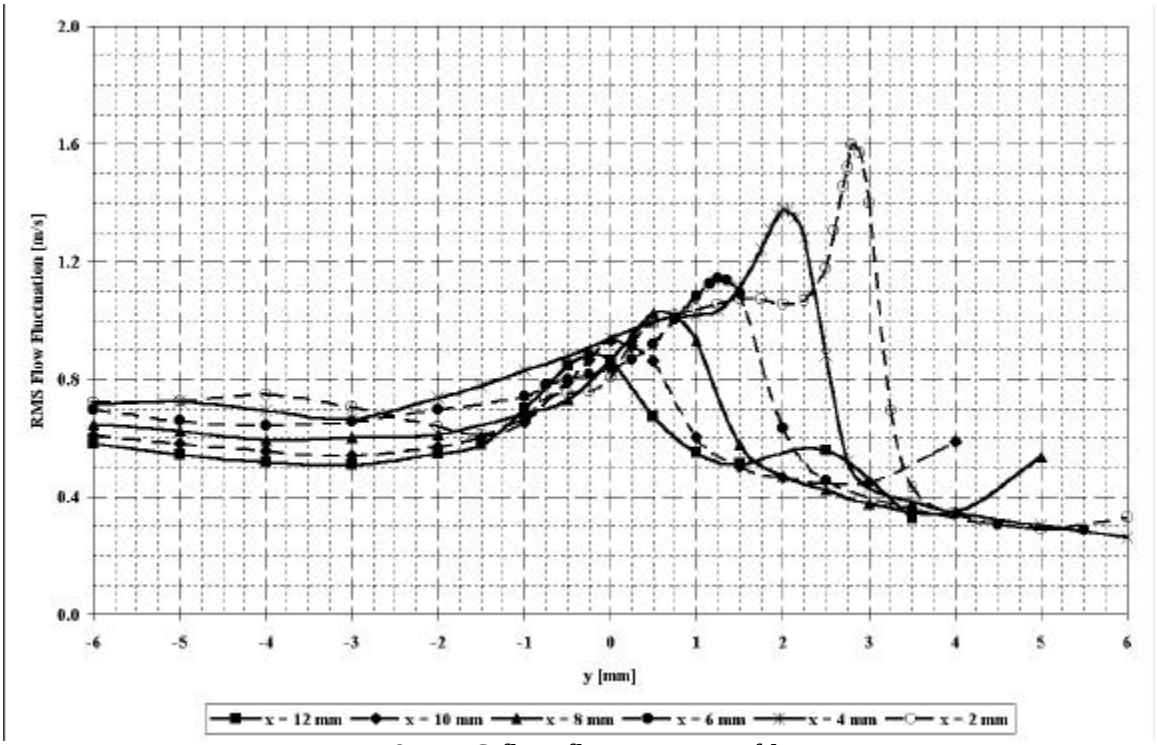

Figure 19: RMS flow fluctuation profiles; t14.

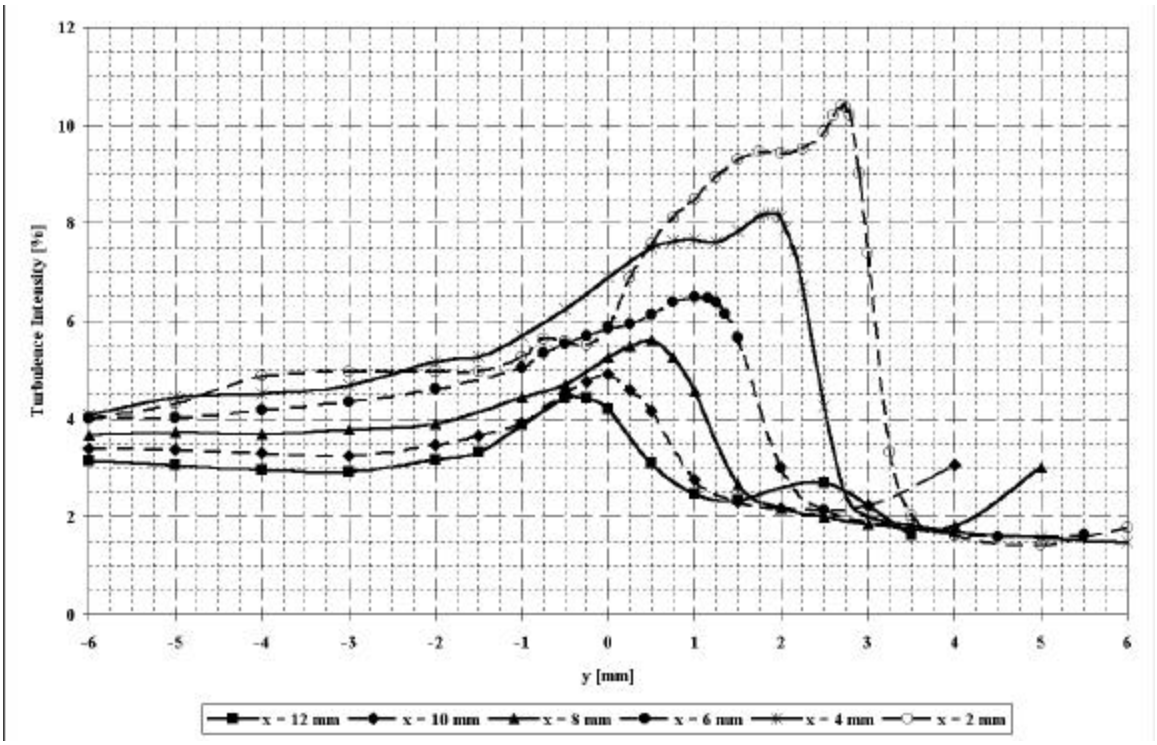

Figure 20: Turbulence intensity profiles; t14.

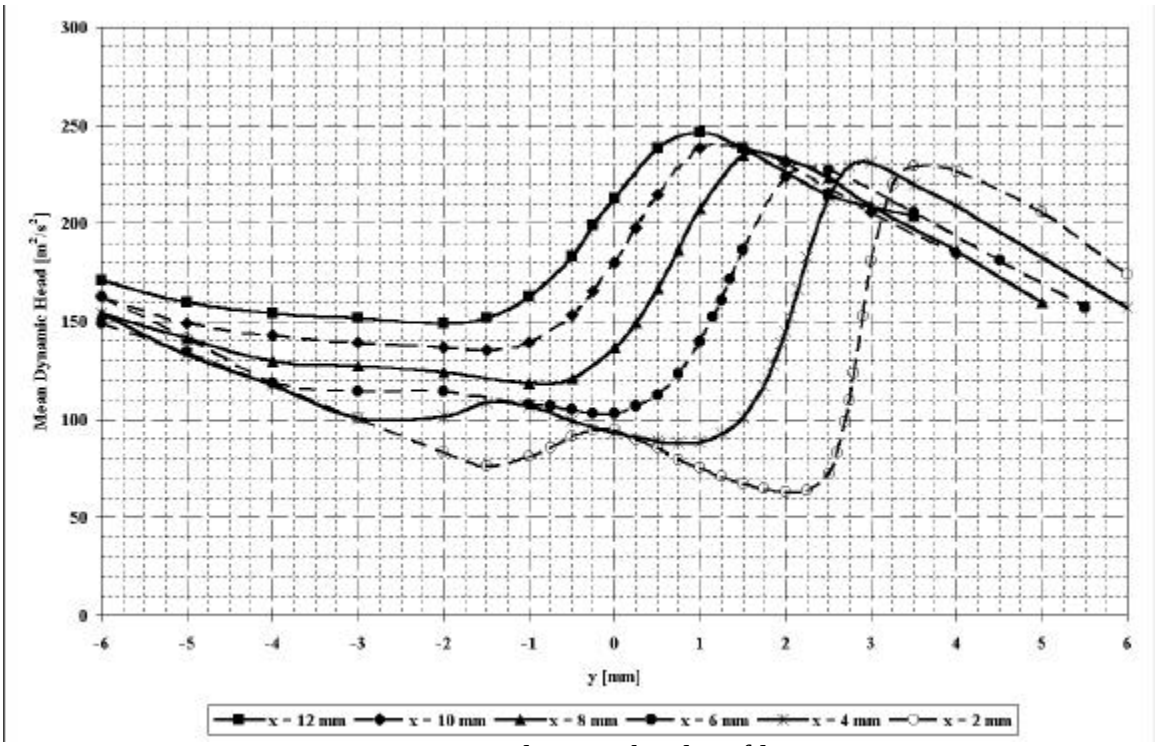

Figure 21: Mean dynamic head profiles; t14.

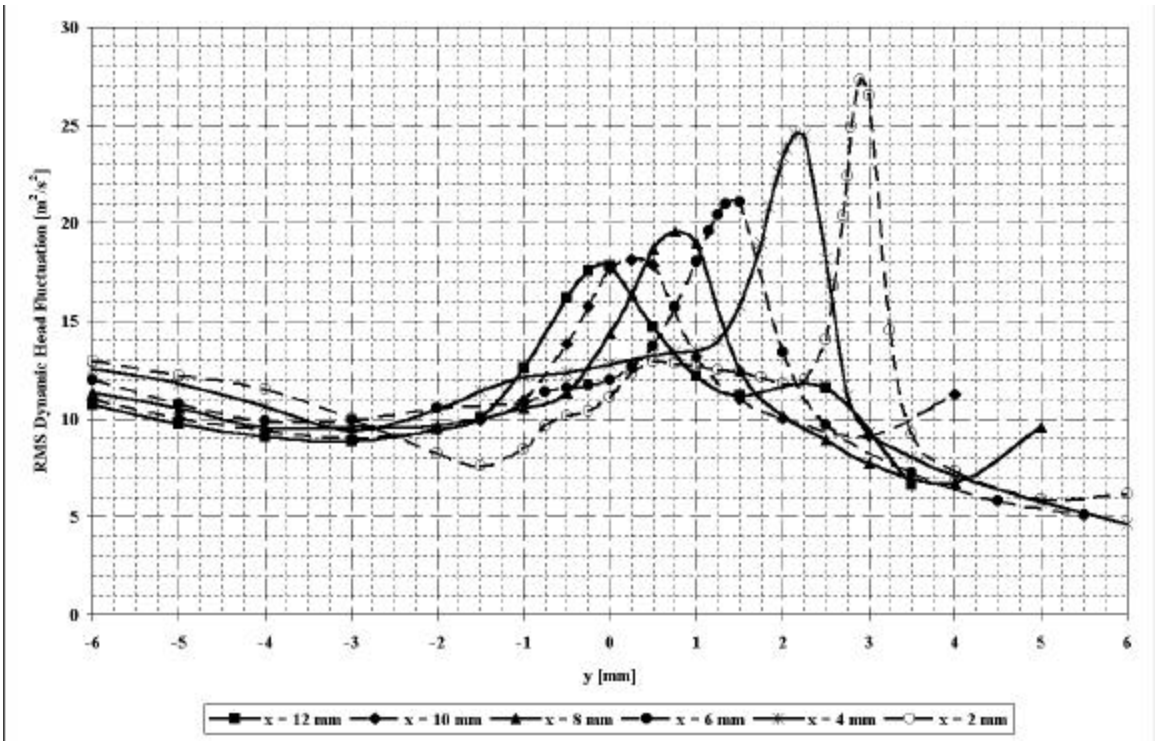

Figure 22: RMS dynamic head fluctuation profiles; t14.

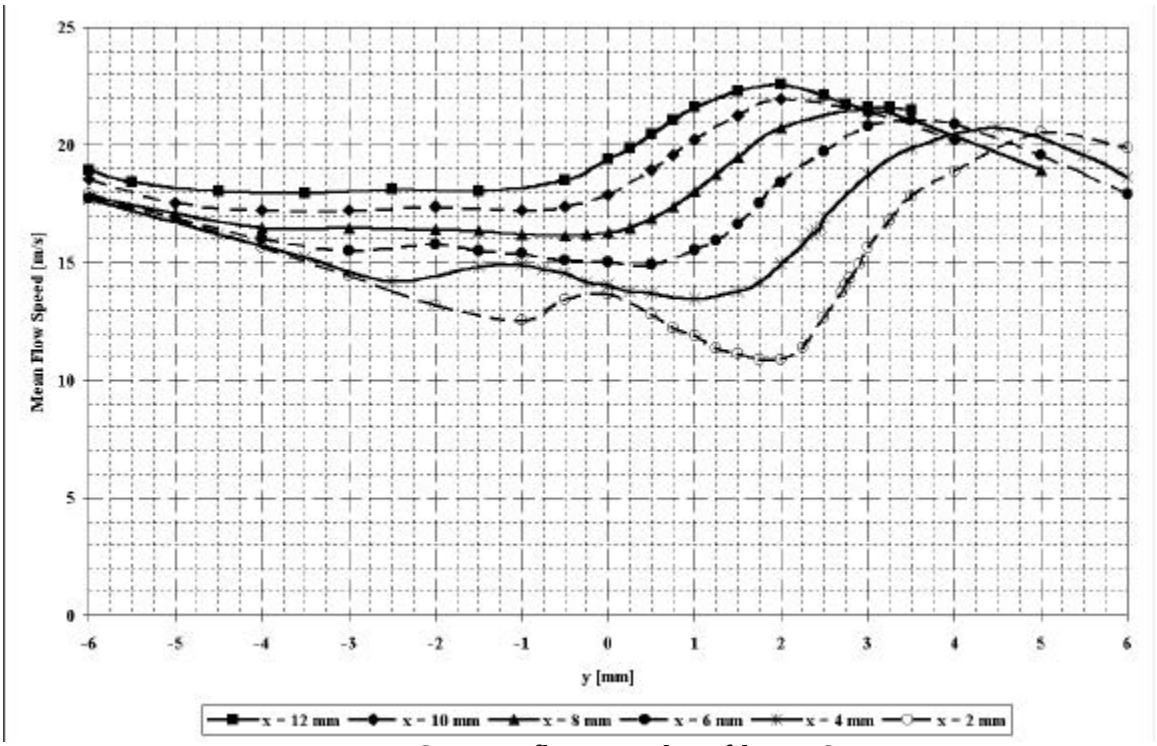

Figure 23: Mean flow speed profiles; t16.

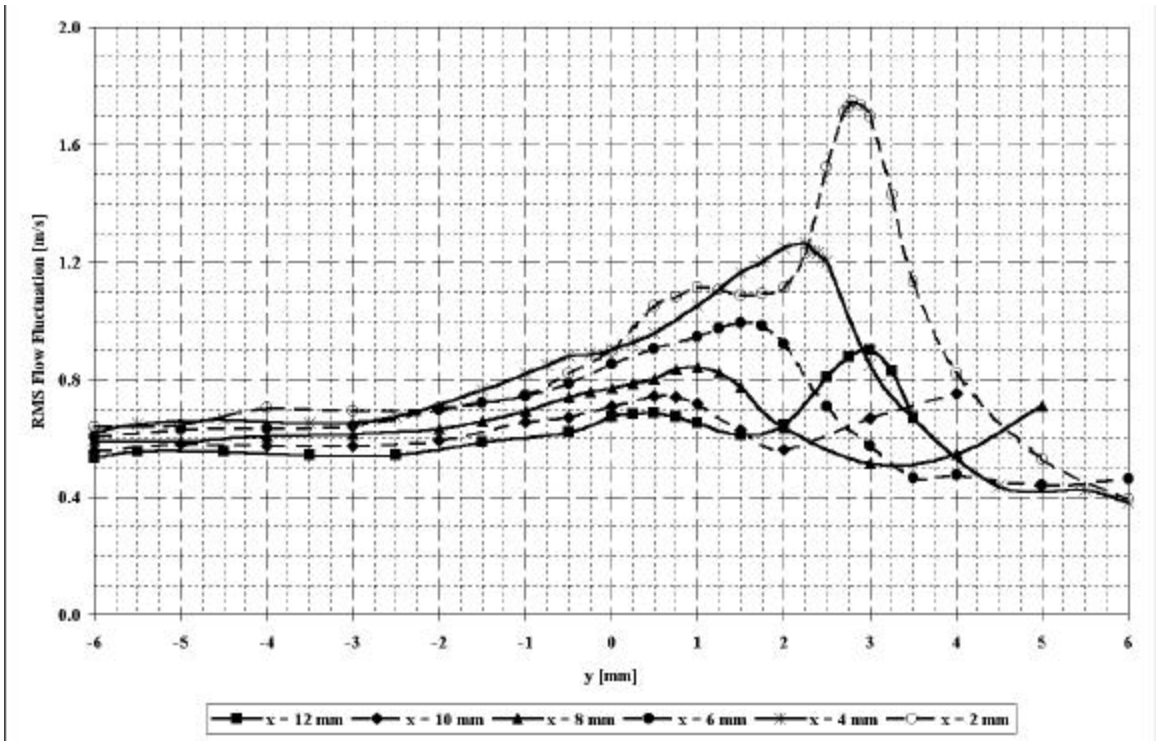

Figure 24: RMS flow fluctuation profiles; t16.

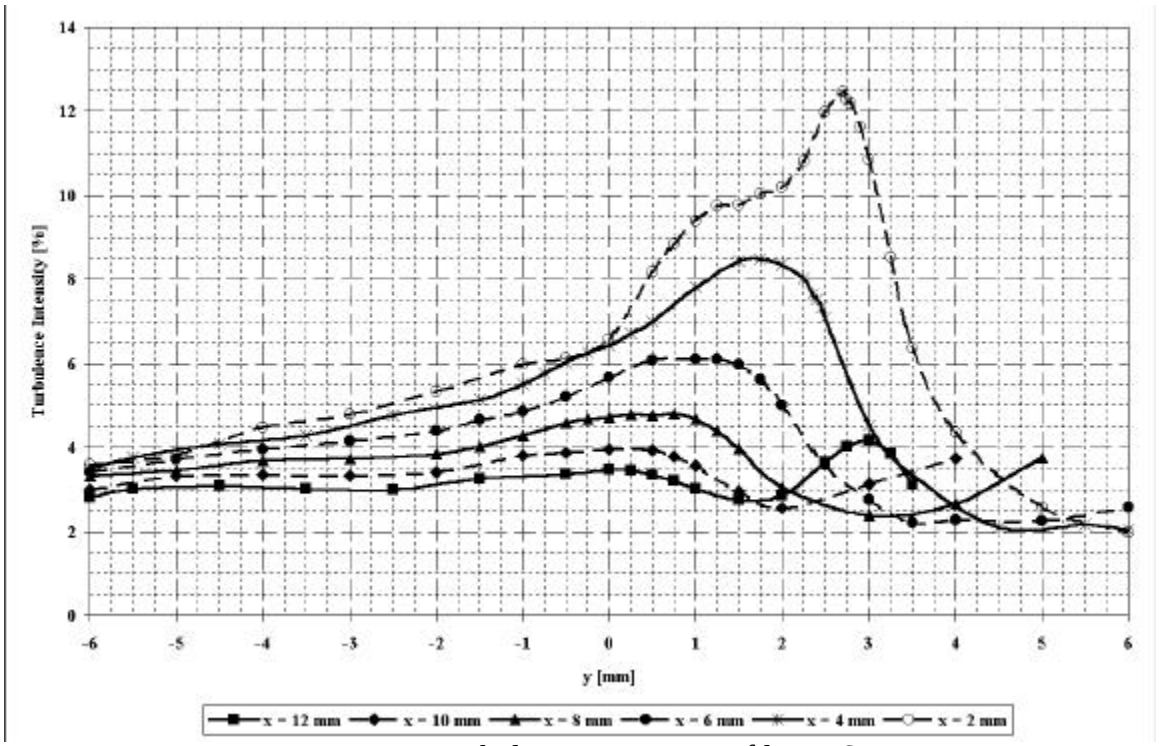

Figure 25: Turbulence intensity profiles; t16.

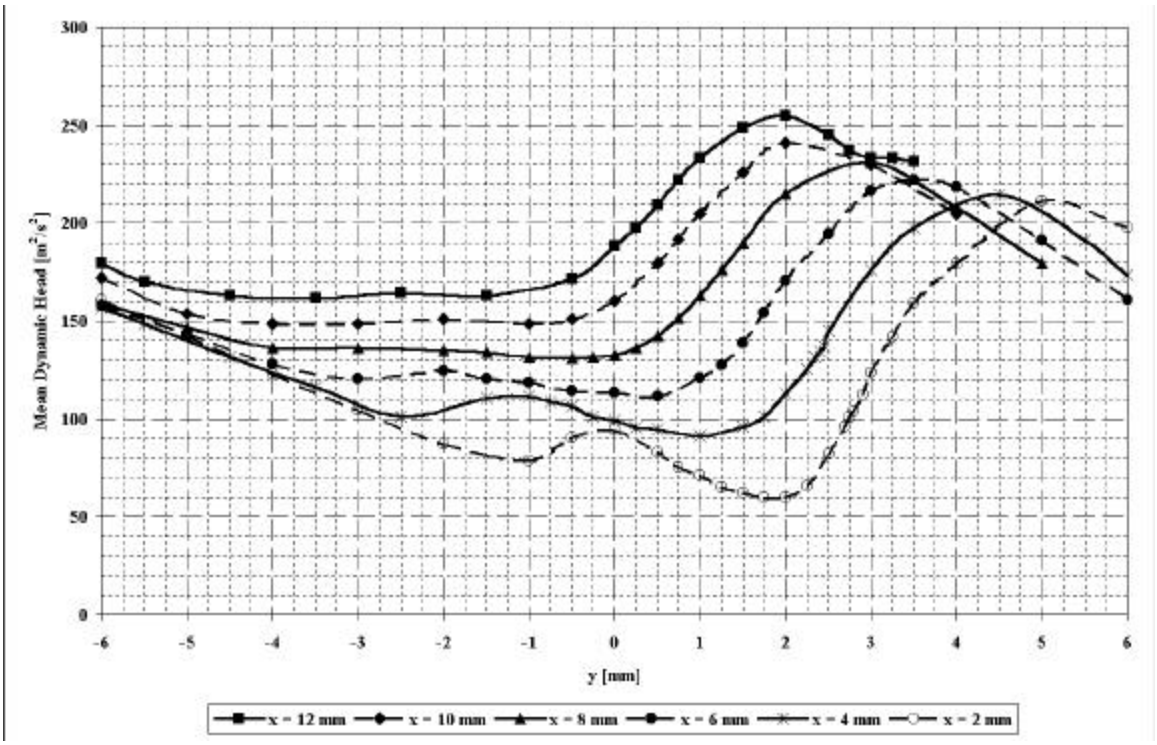

Figure 26: Mean dynamic head profiles; t16.

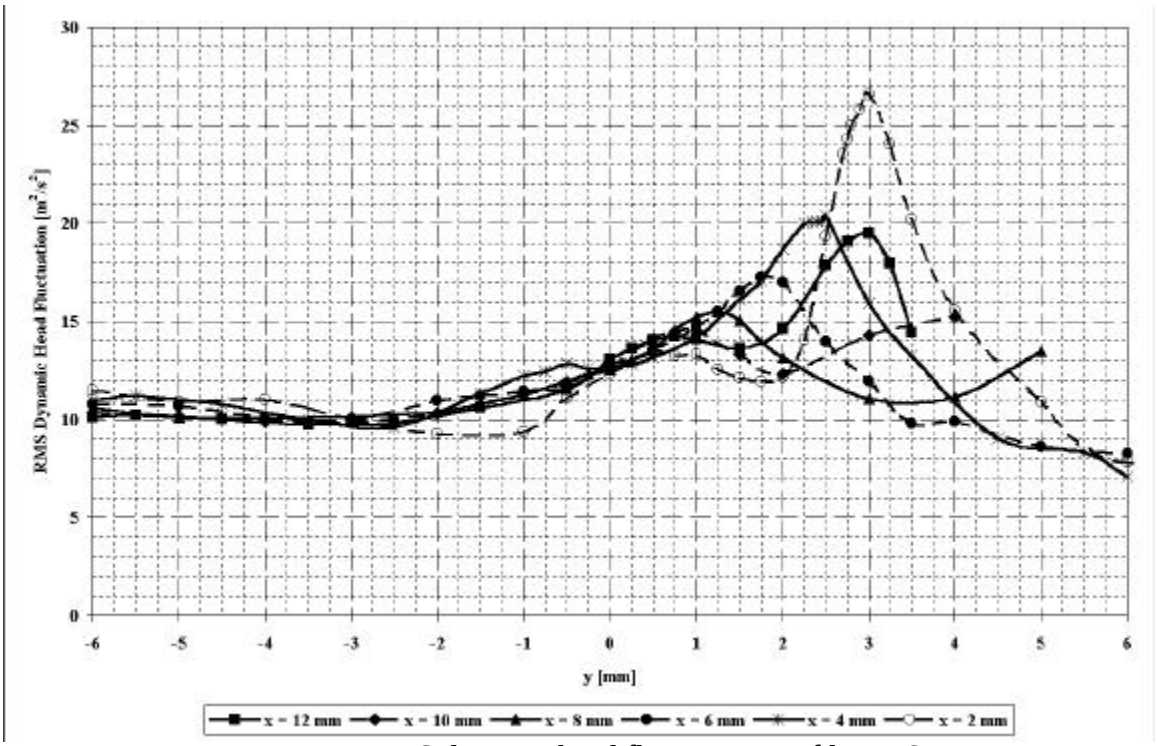

Figure 27: RMS dynamic head fluctuation profiles; t16.

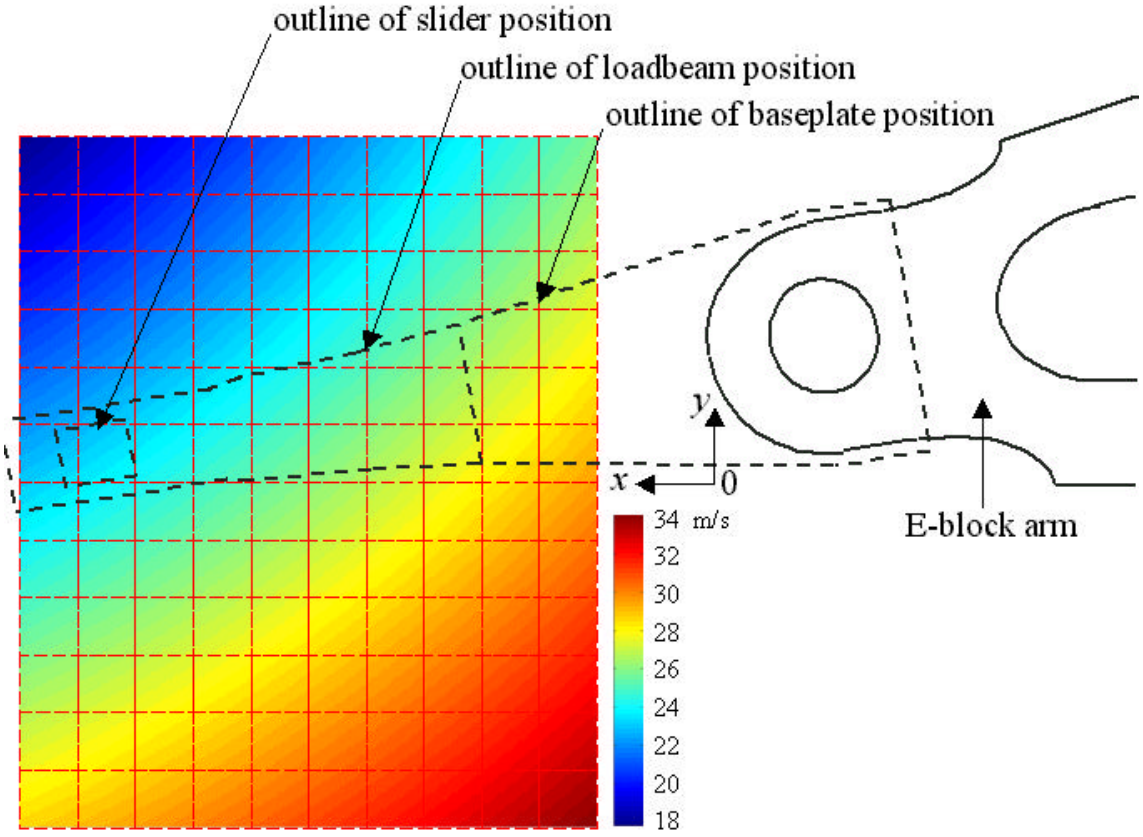

(a) Disk surface speed, full scale

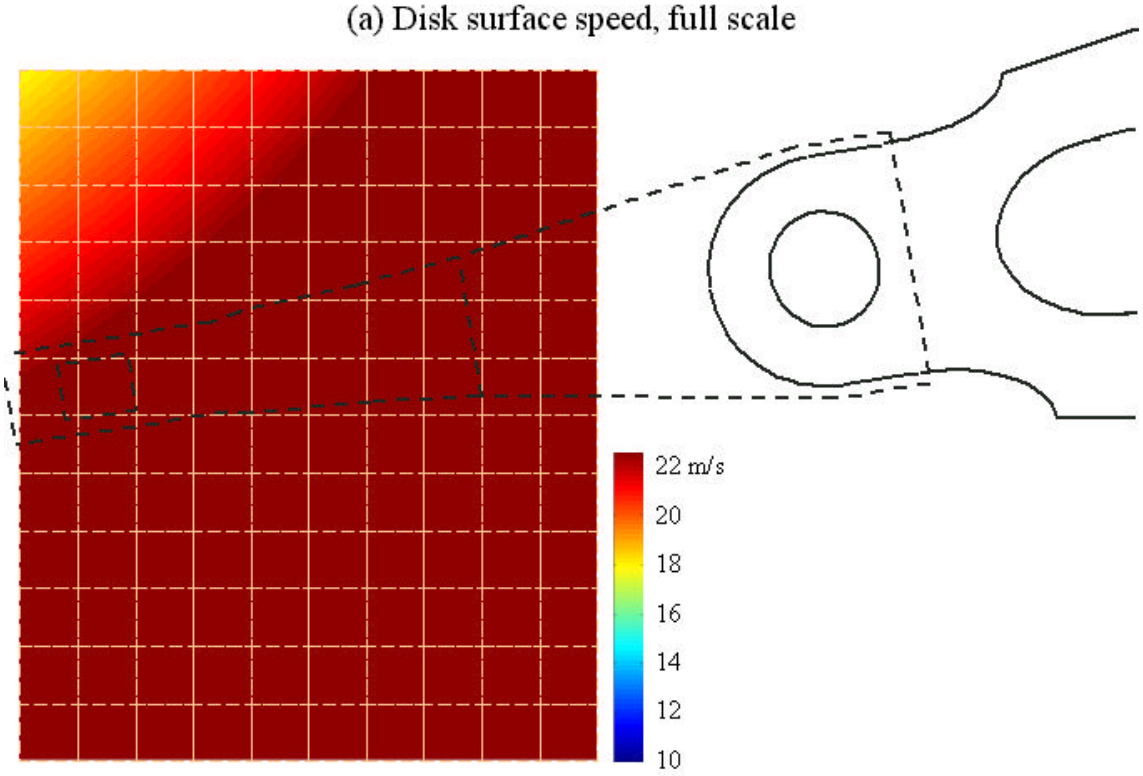

(b) Disk surface speed, clipped scale

Figure 28: Disk surface speed.

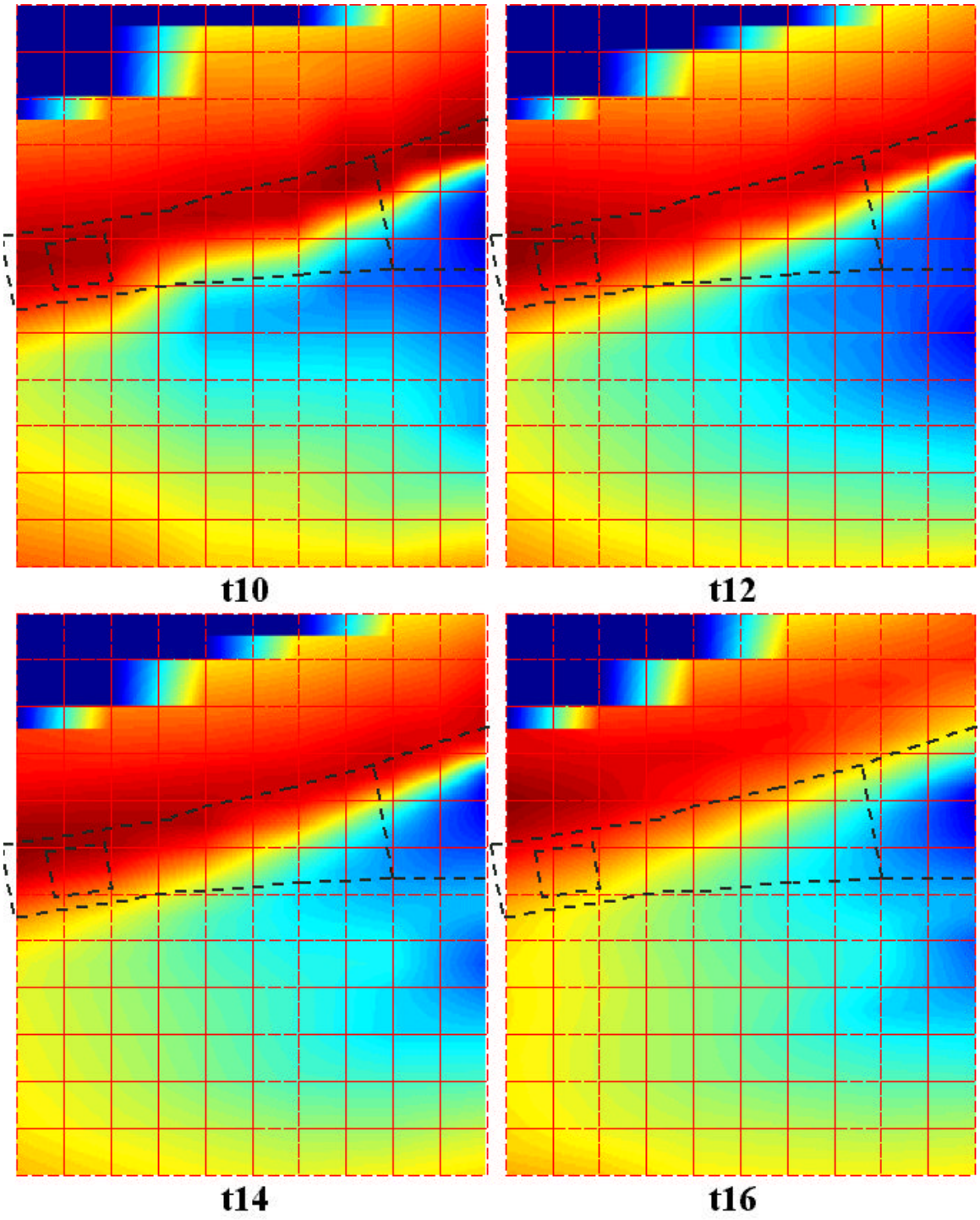

Figure 29: Mean flow speed distributions; different scales.

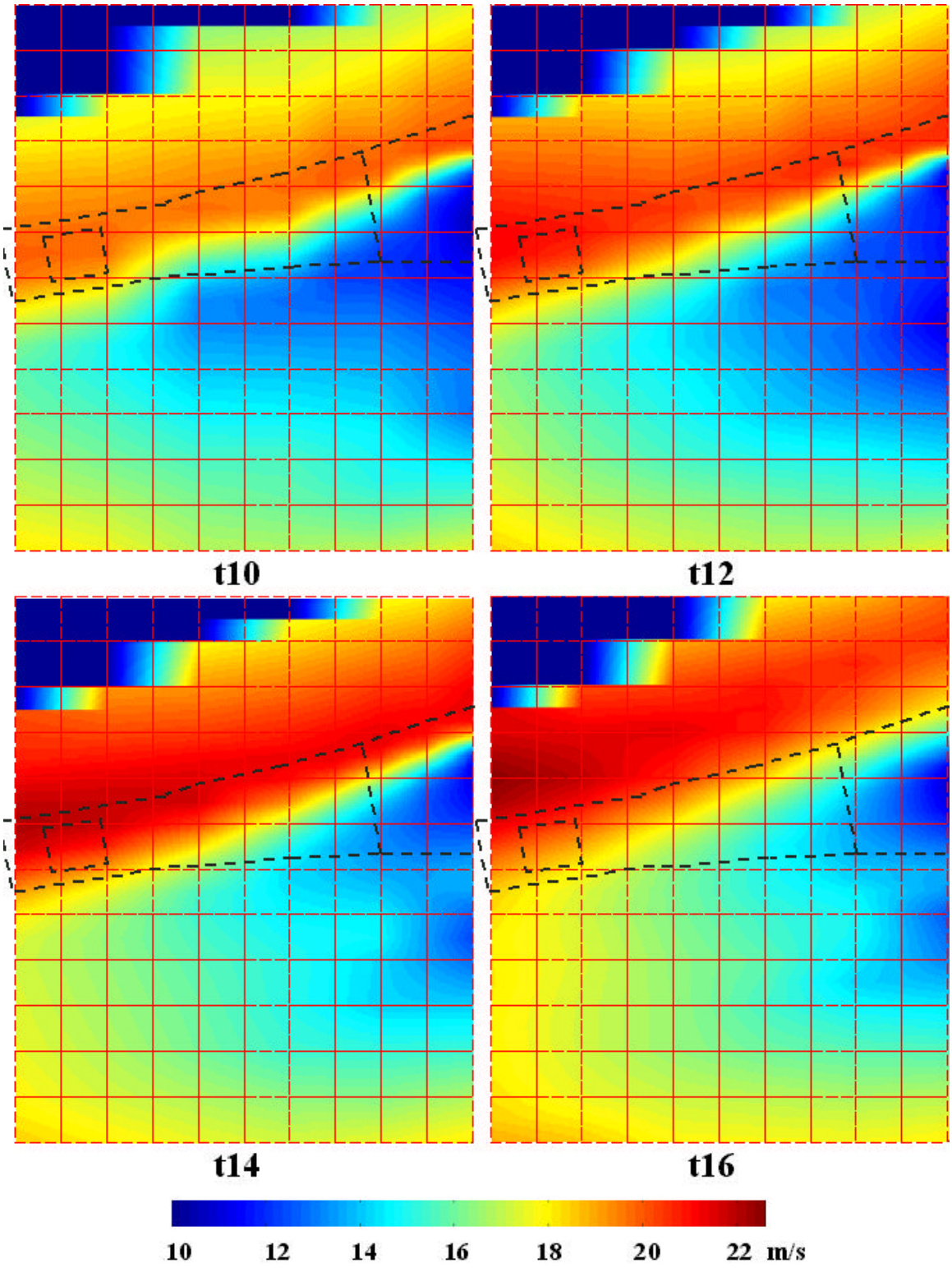

Figure 30: Mean flow speed distributions; same scale.

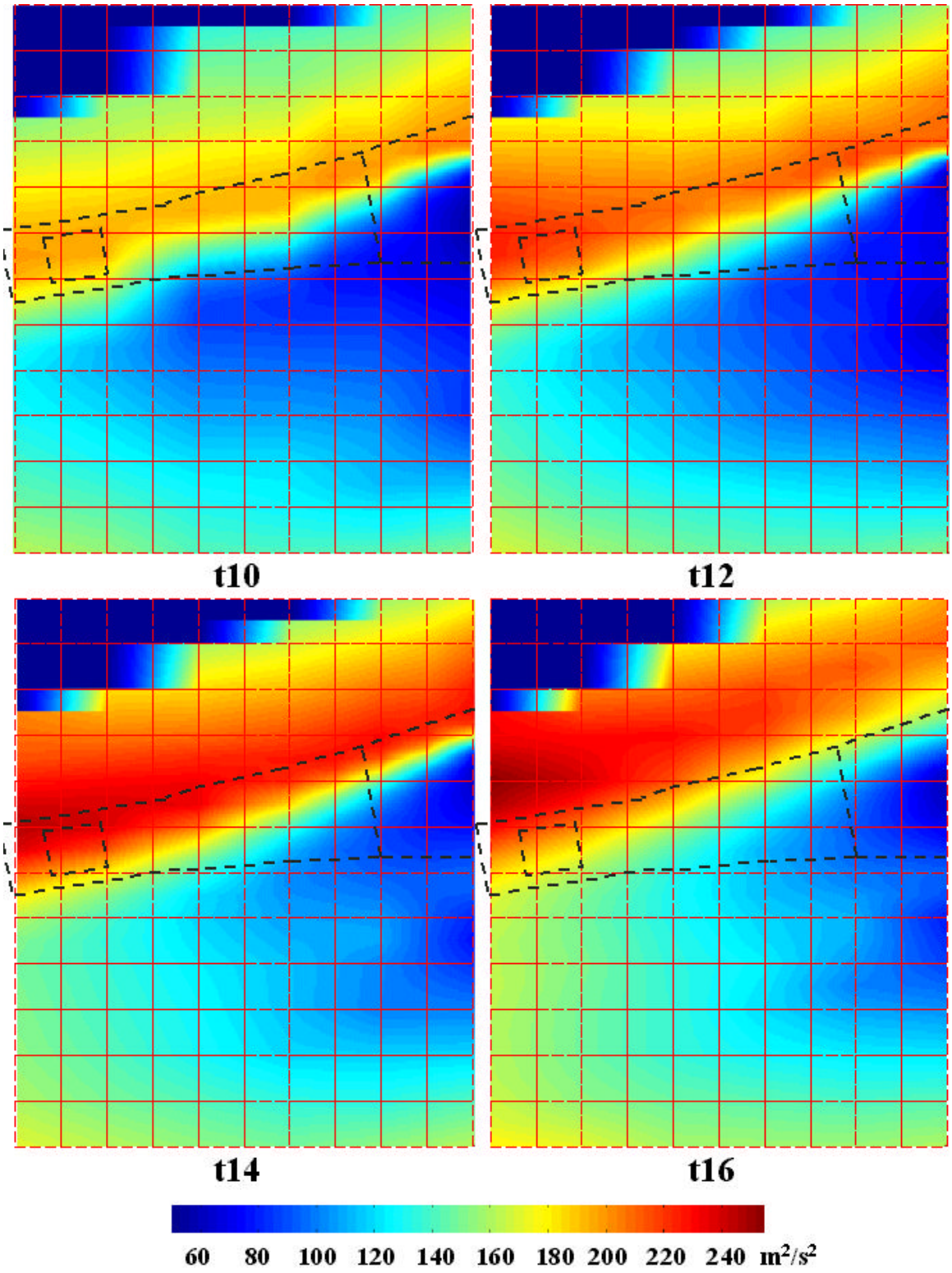

Figure 31: Mean dynamic head distributions.

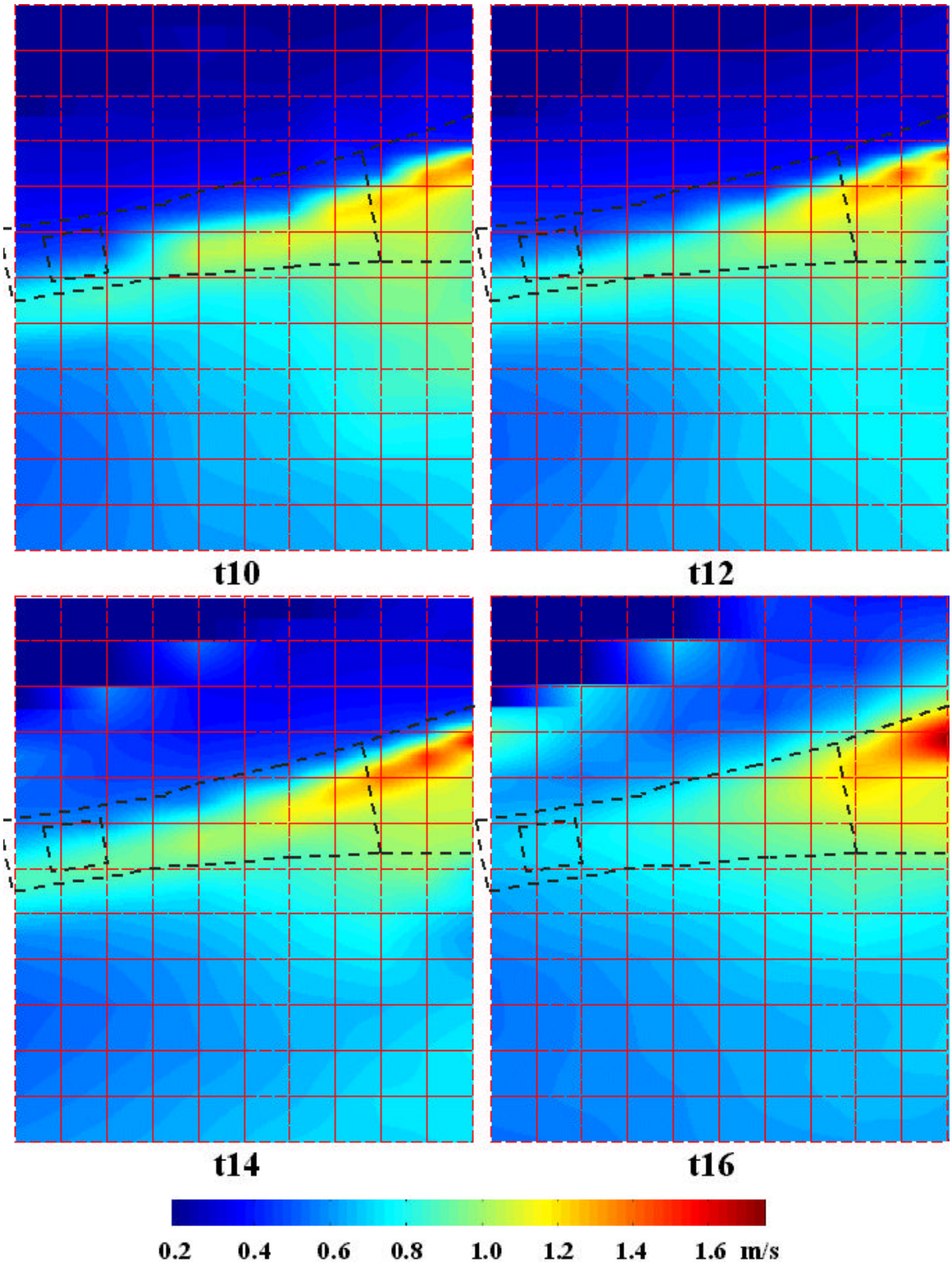

Figure 32: RMS flow fluctuation distributions.

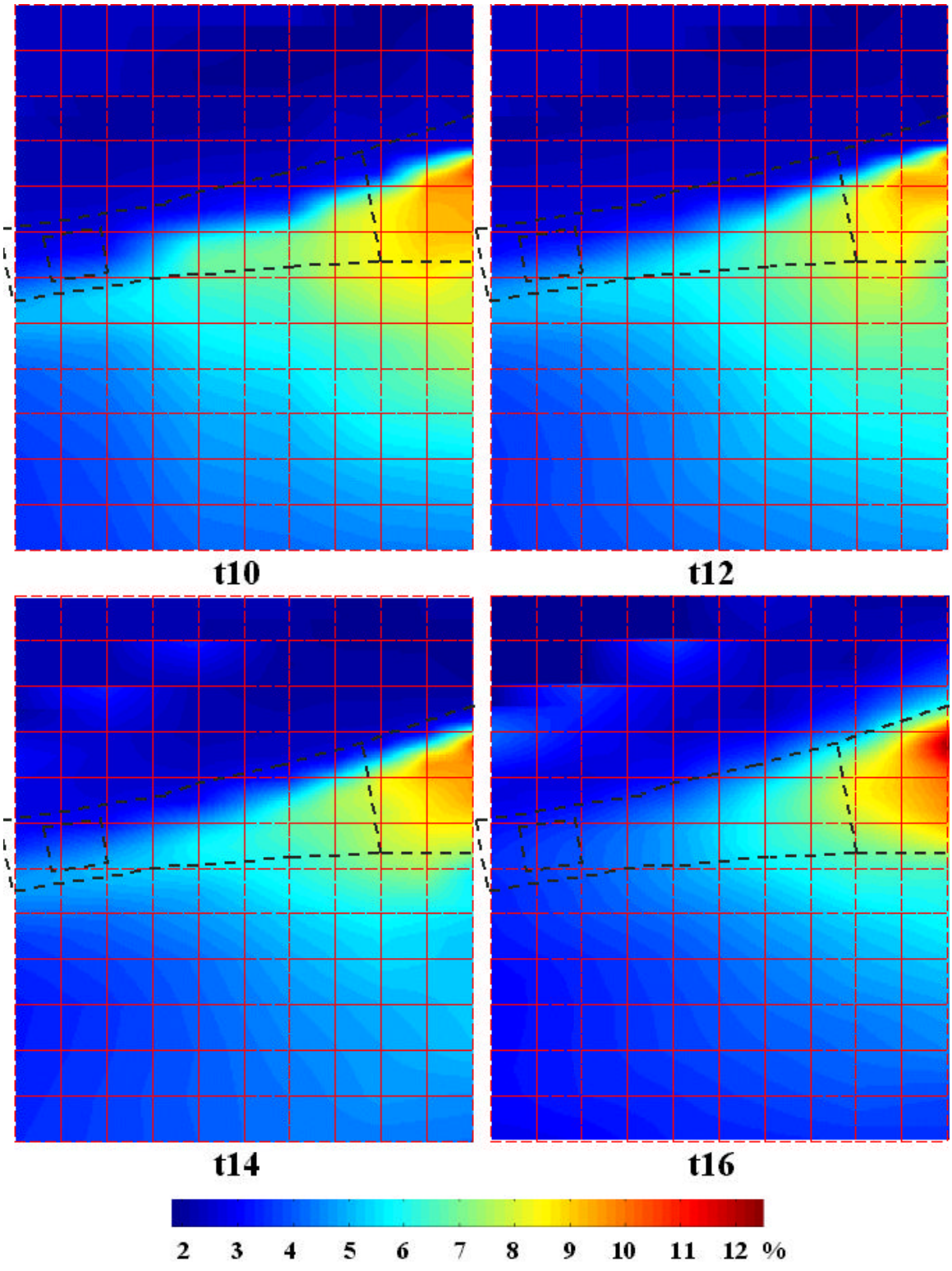

Figure 33: Turbulence intensity distributions.

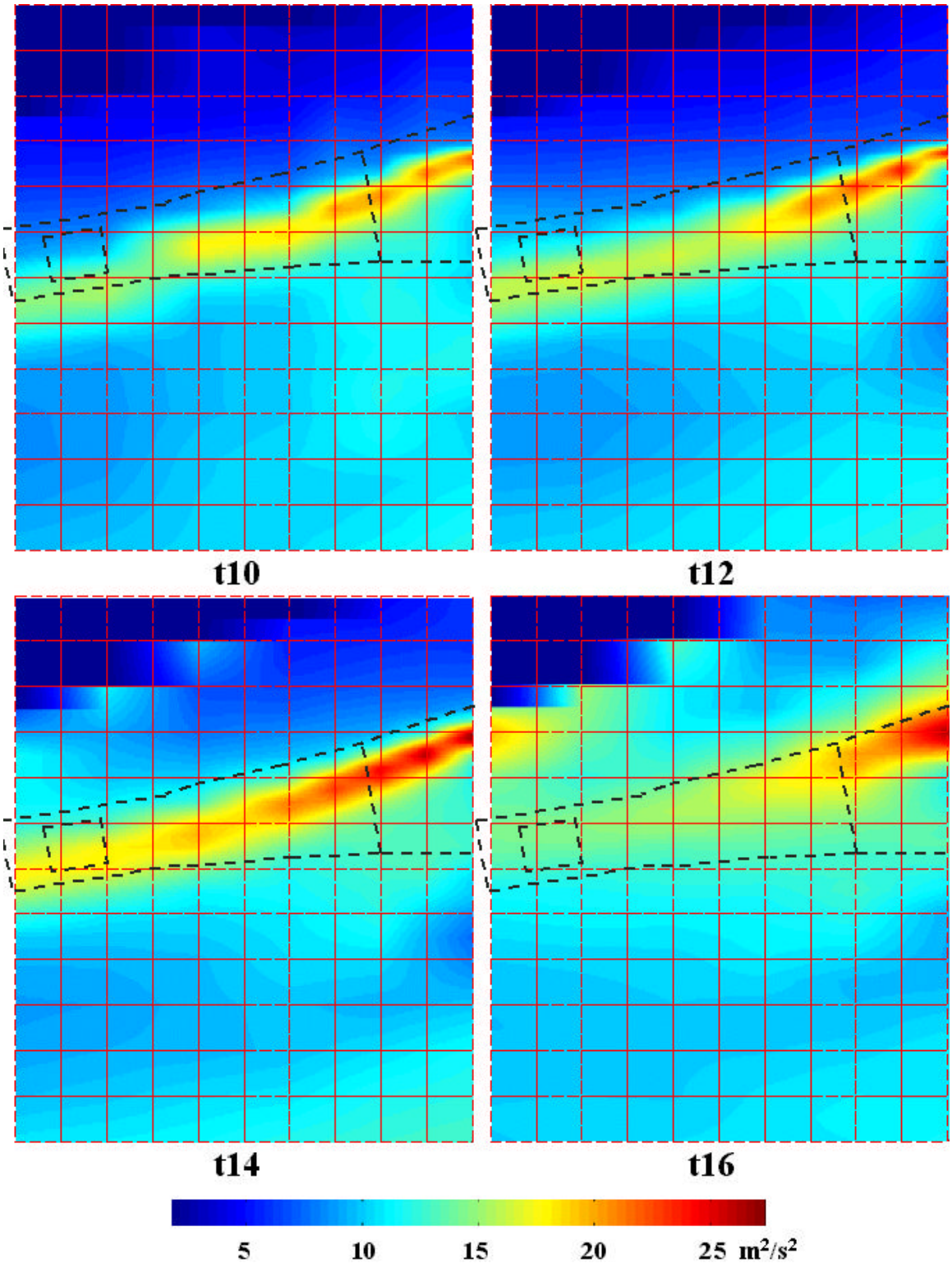

Figure 34: RMS dynamic head fluctuation distributions.

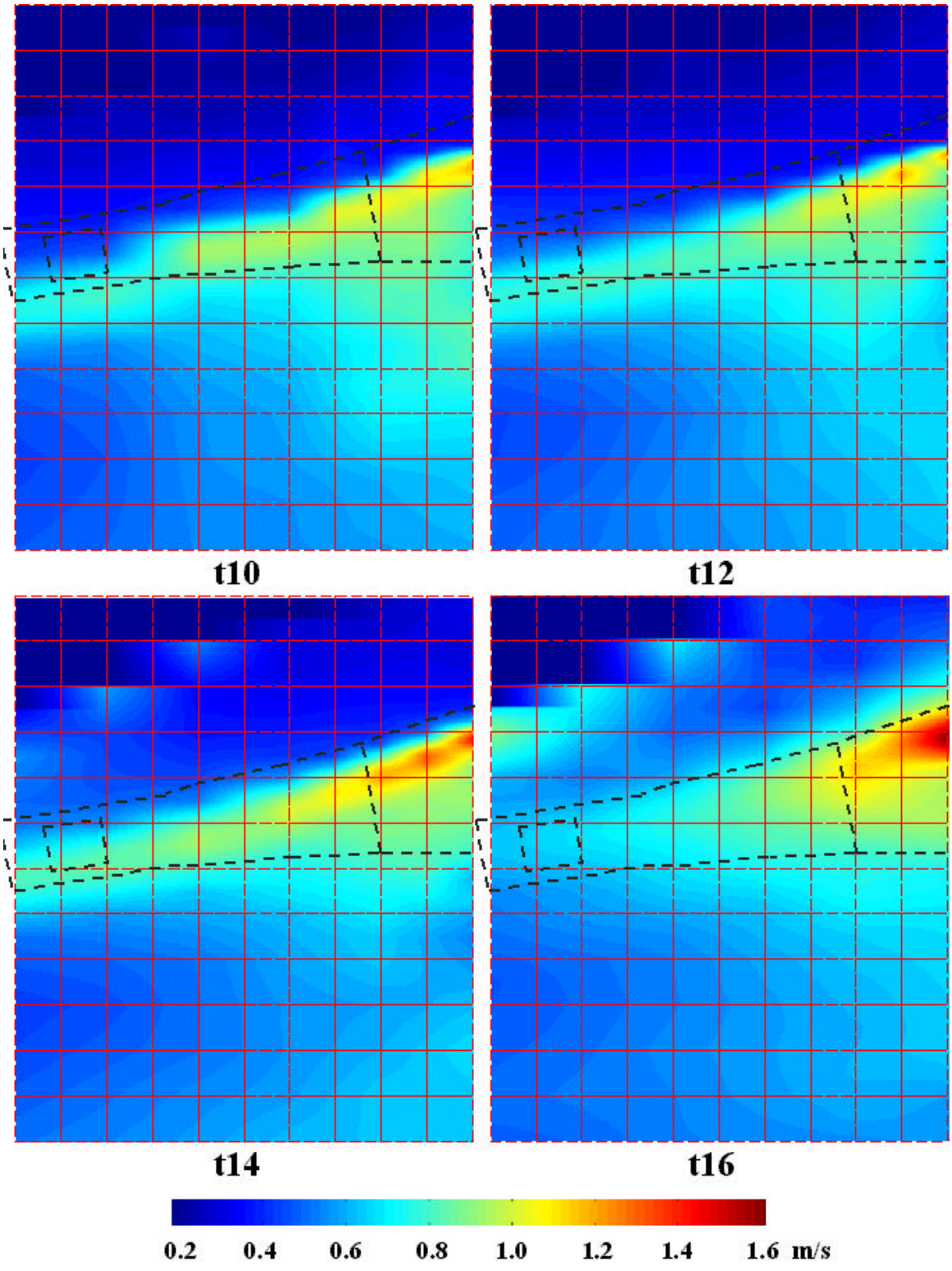

Figure 35: Distributions of 0-2 kHz component of RMS flow fluctuation.

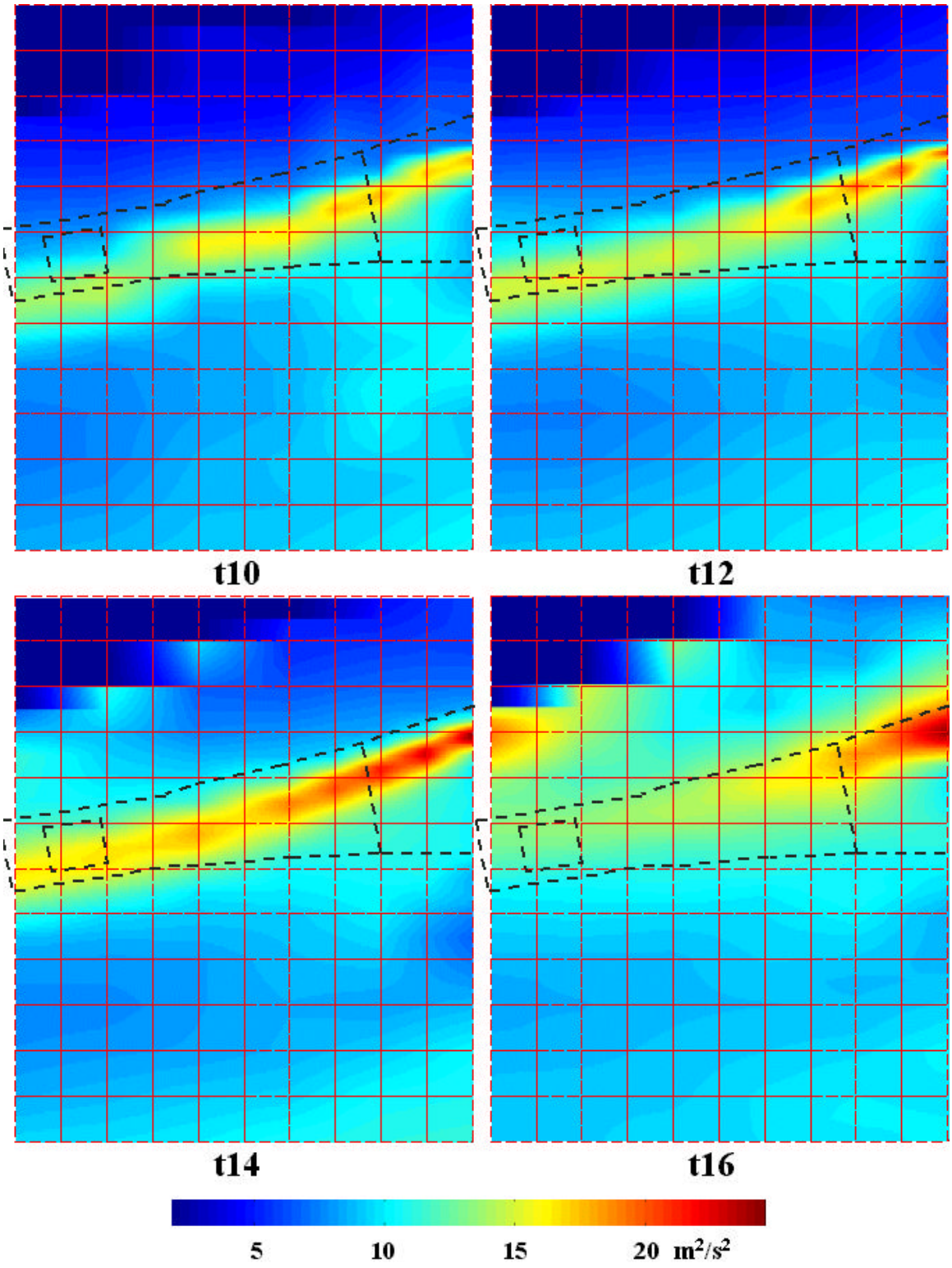

Figure 36: Distributions of 0-2 kHz component of RMS dynamic head fluctuation.

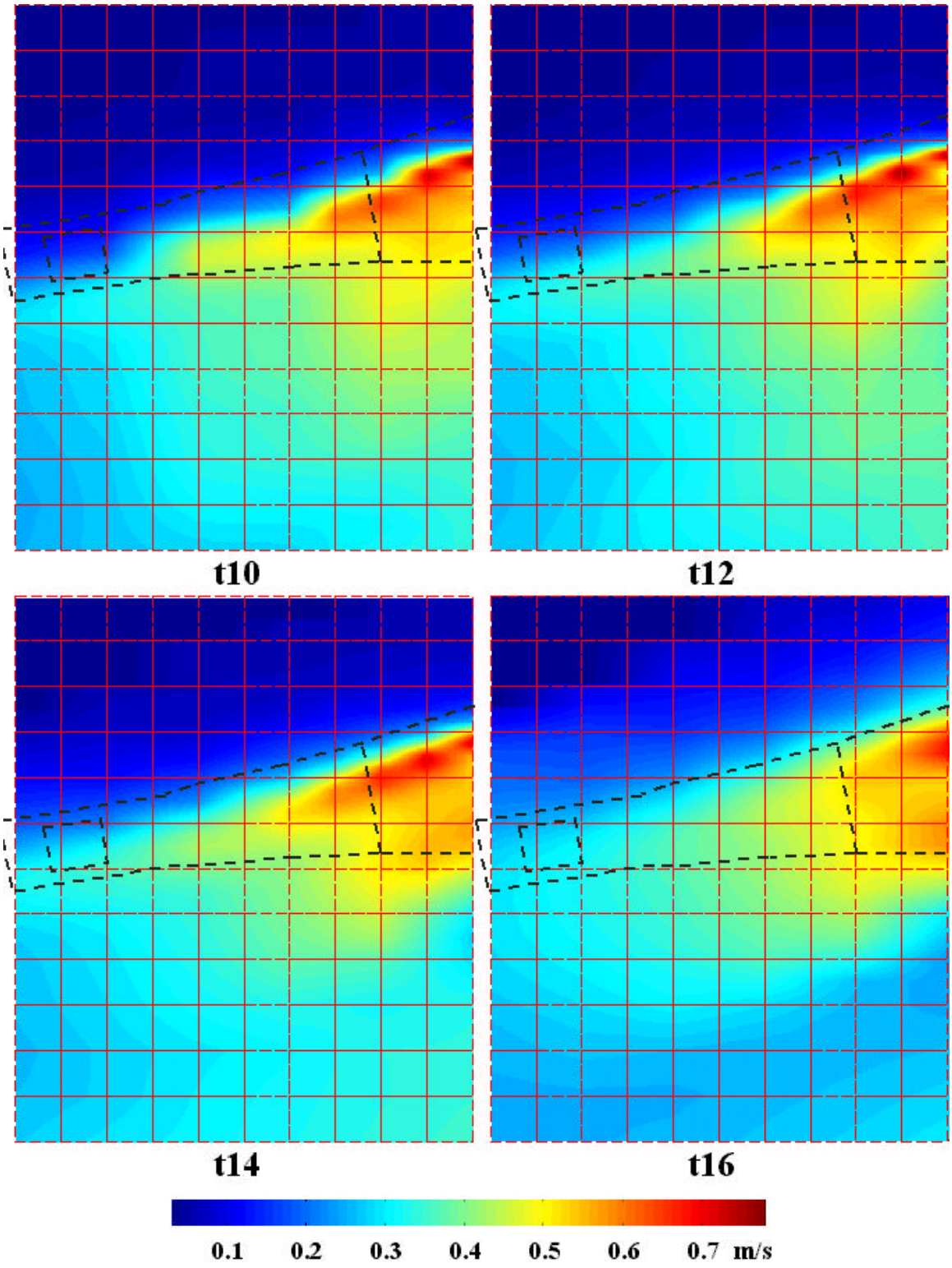

Figure 37: Distributions of 2-20 kHz component of RMS flow fluctuation.

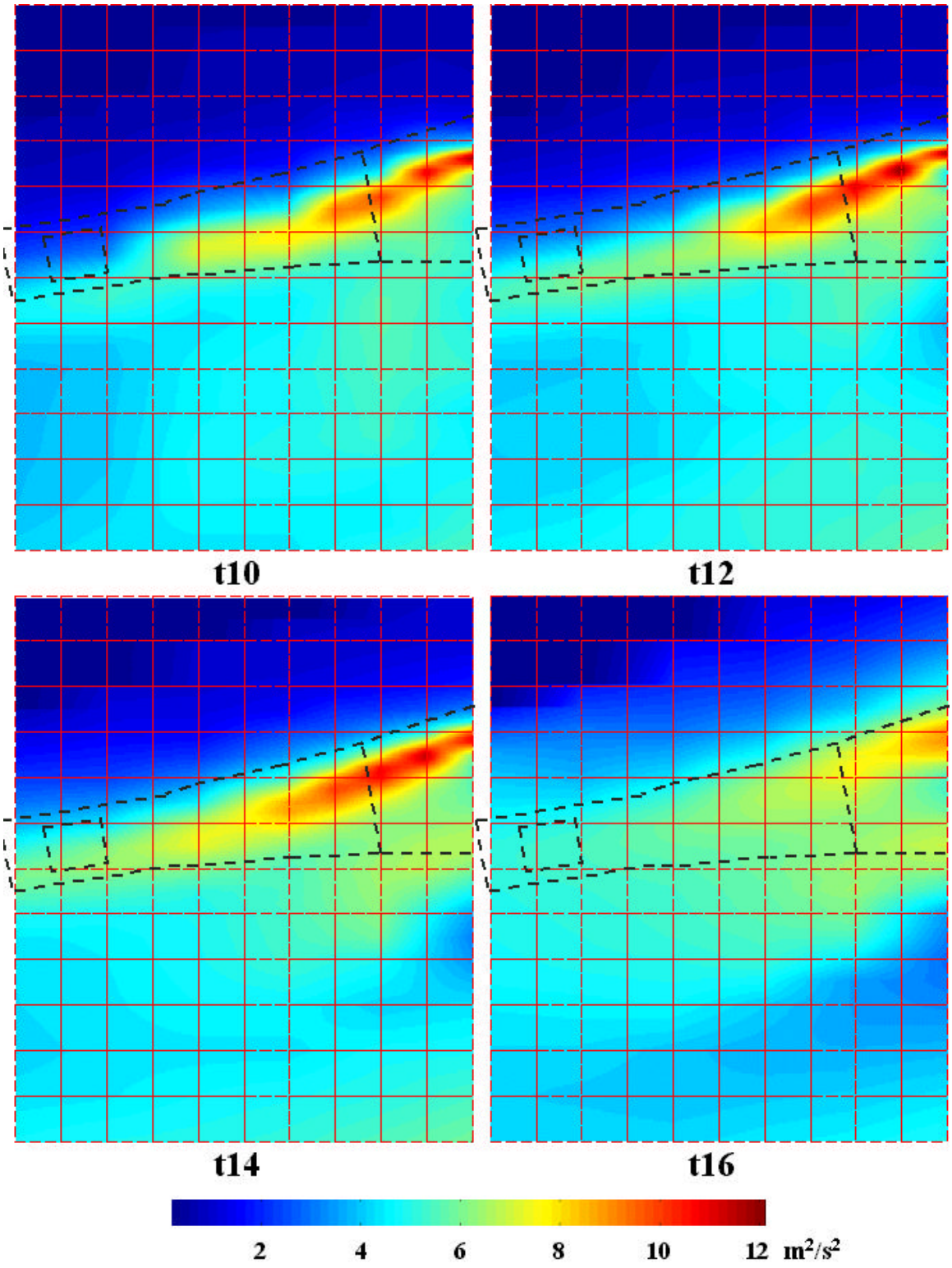

Figure 38: Distributions of 2-20 kHz component of RMS dynamic head fluctuation.

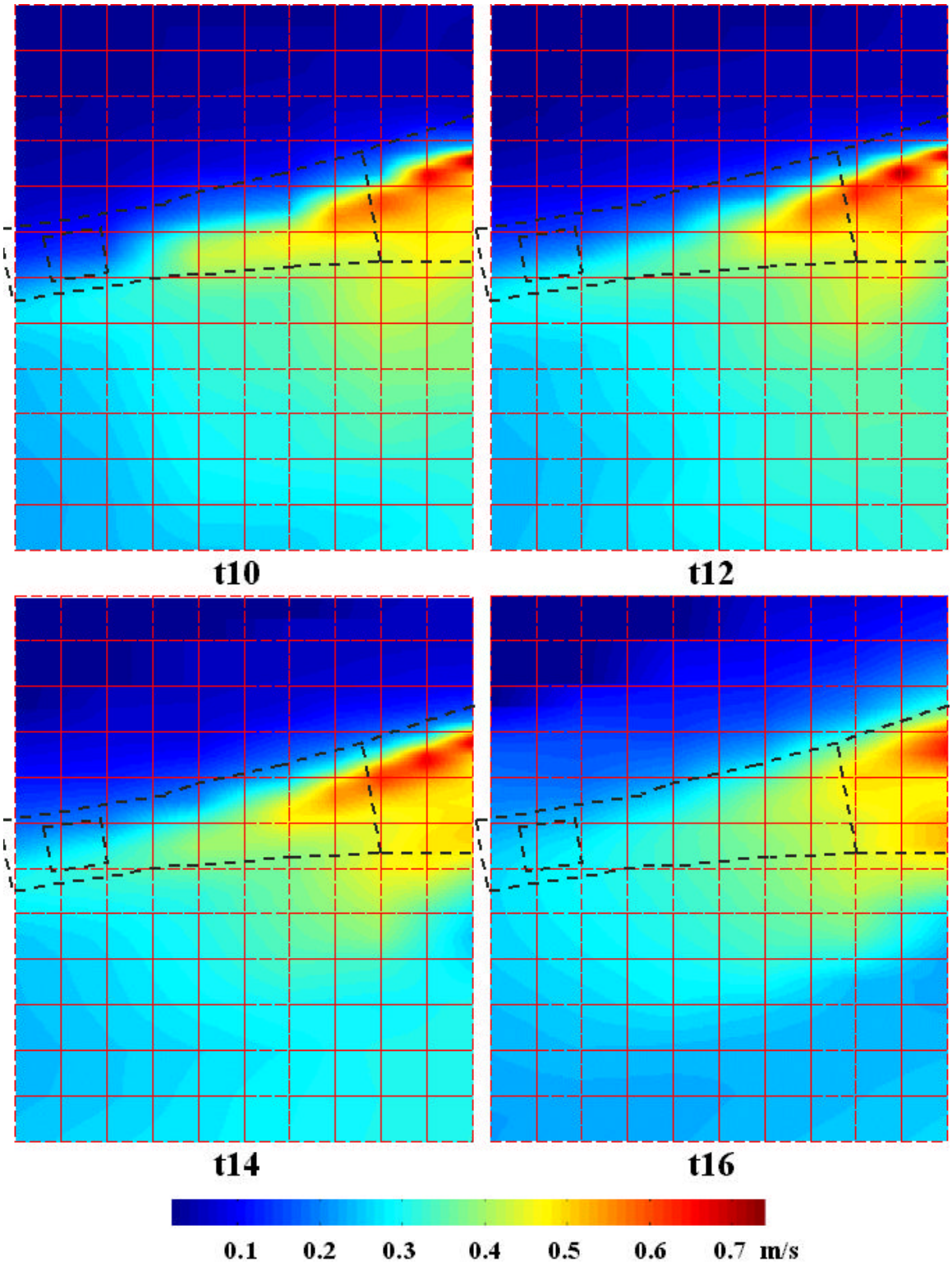

Figure 39: Distributions of 2-6 kHz component of RMS flow fluctuation.

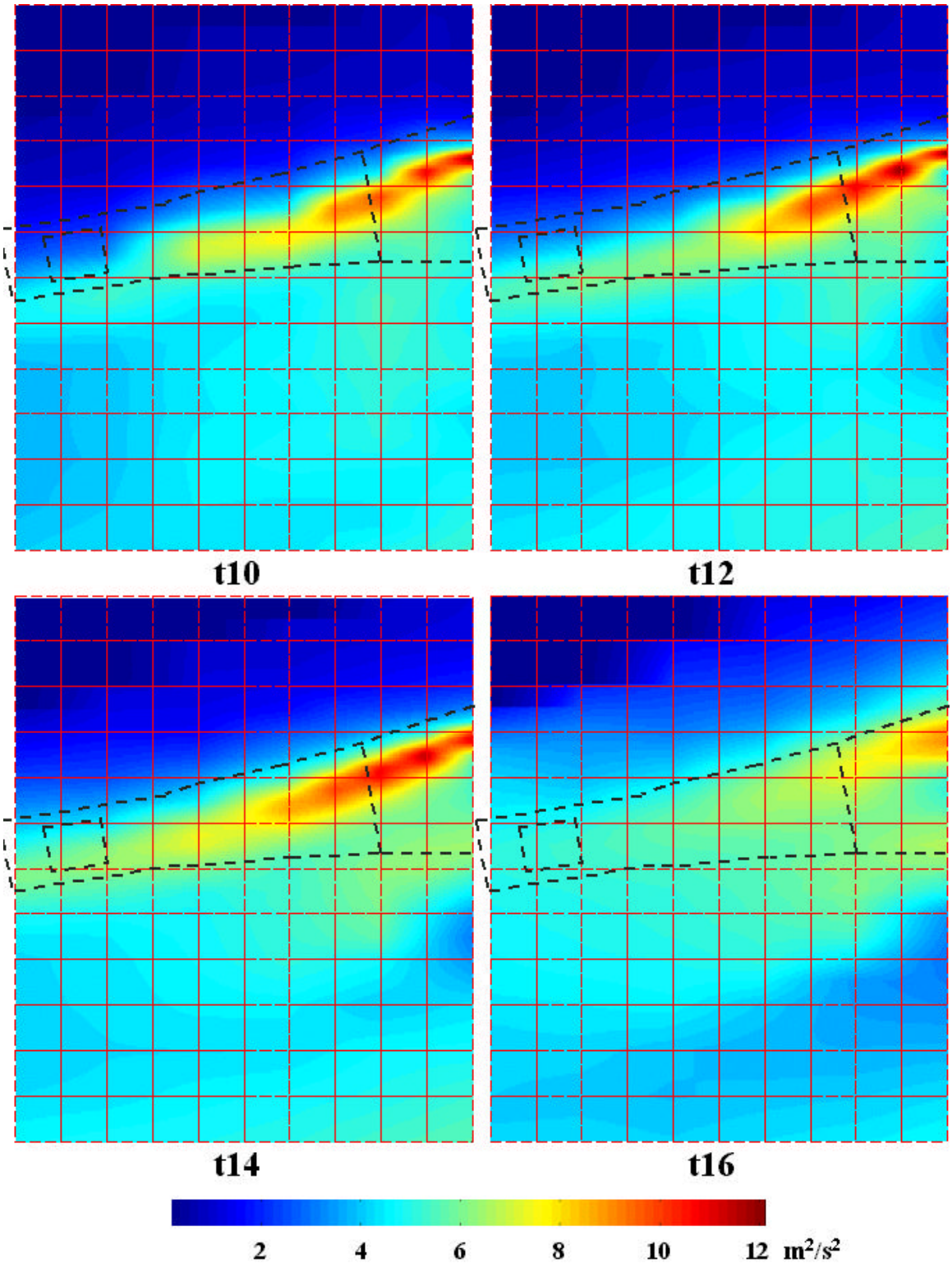

Figure 40: Distributions of 2-6 kHz component of RMS dynamic head fluctuation.

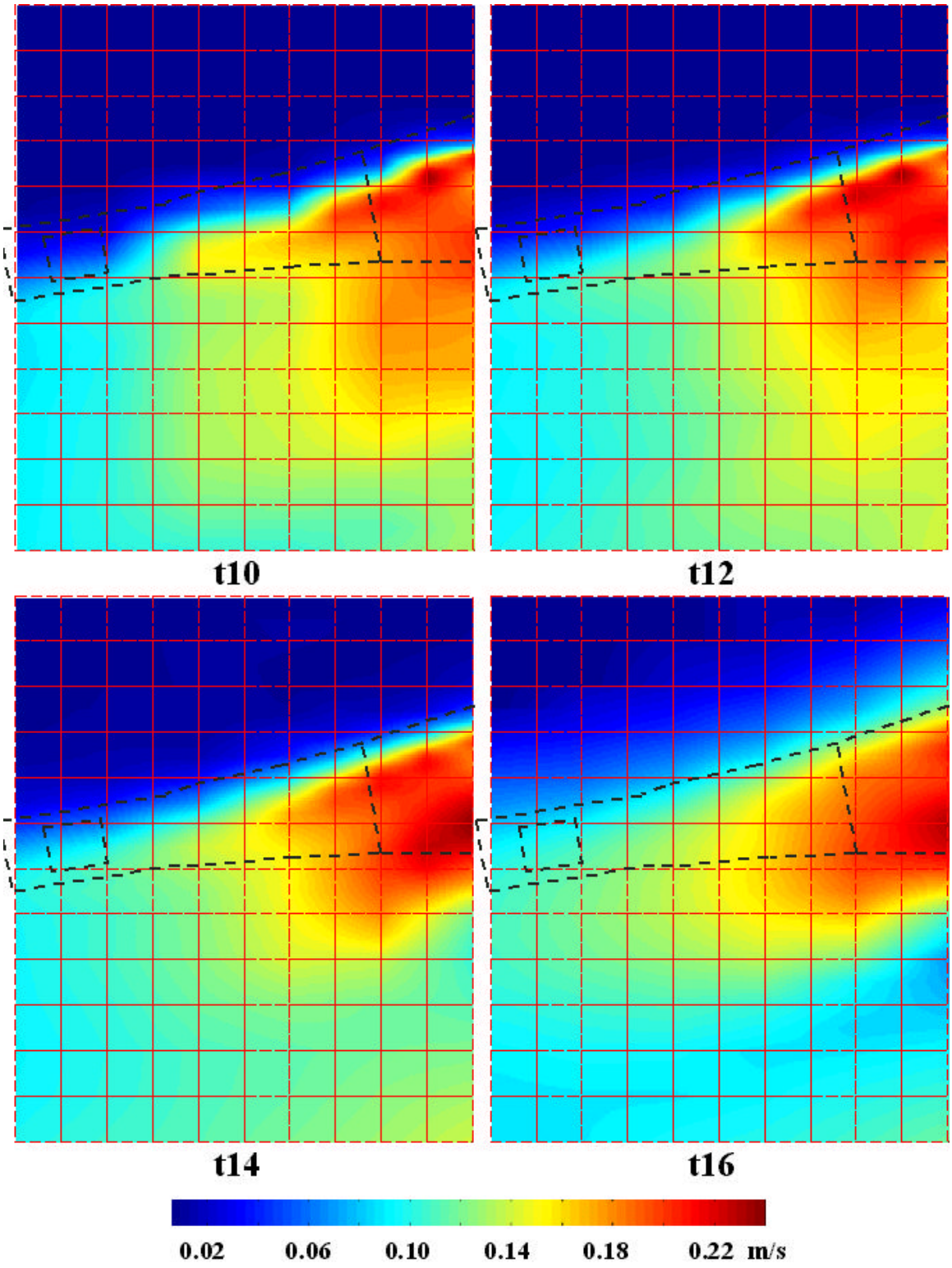

Figure 41: Distributions of 6-10 kHz component of RMS flow fluctuation.

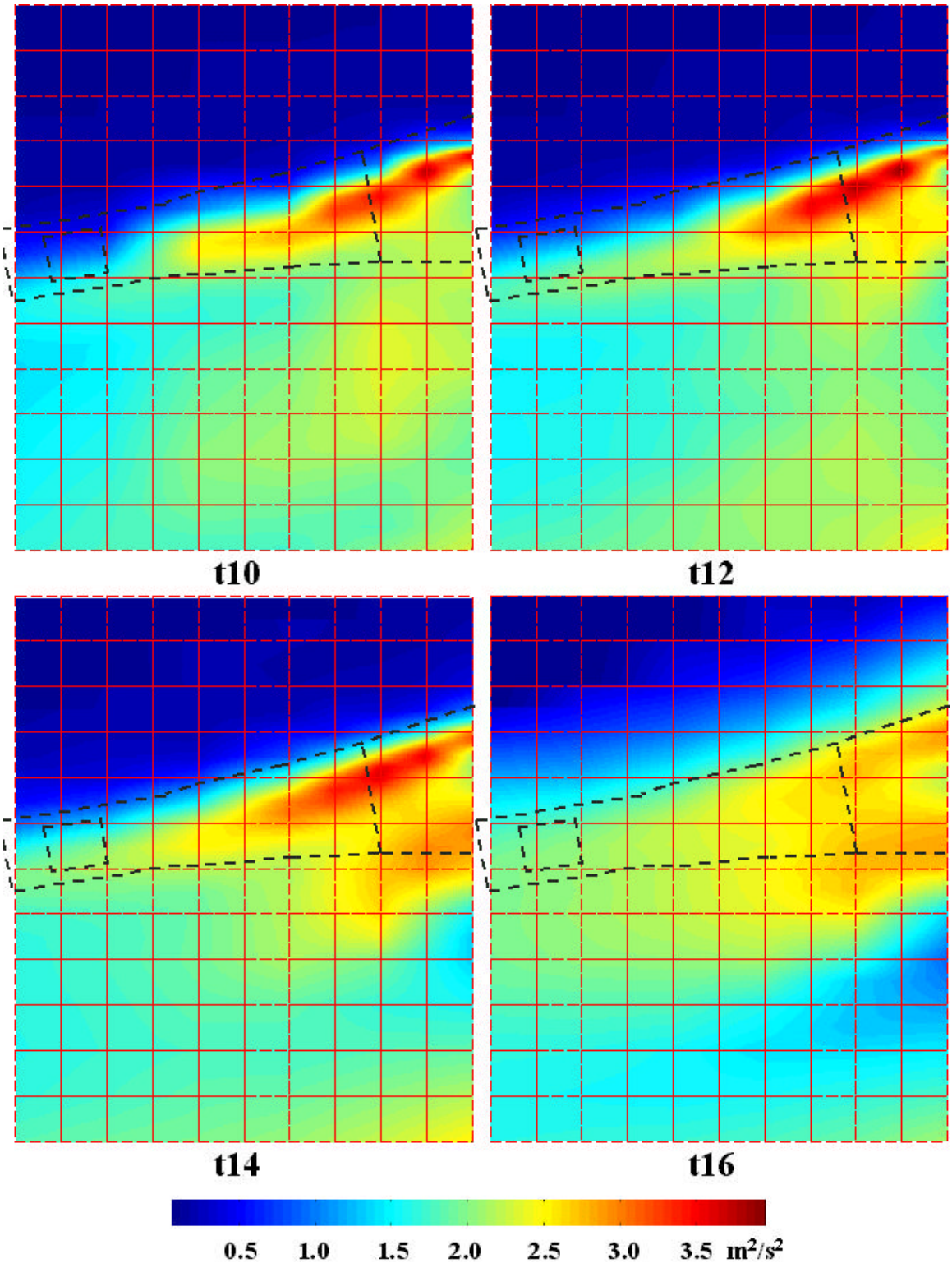

Figure 42: Distributions of 6-10 kHz component of RMS dynamic head fluctuation.

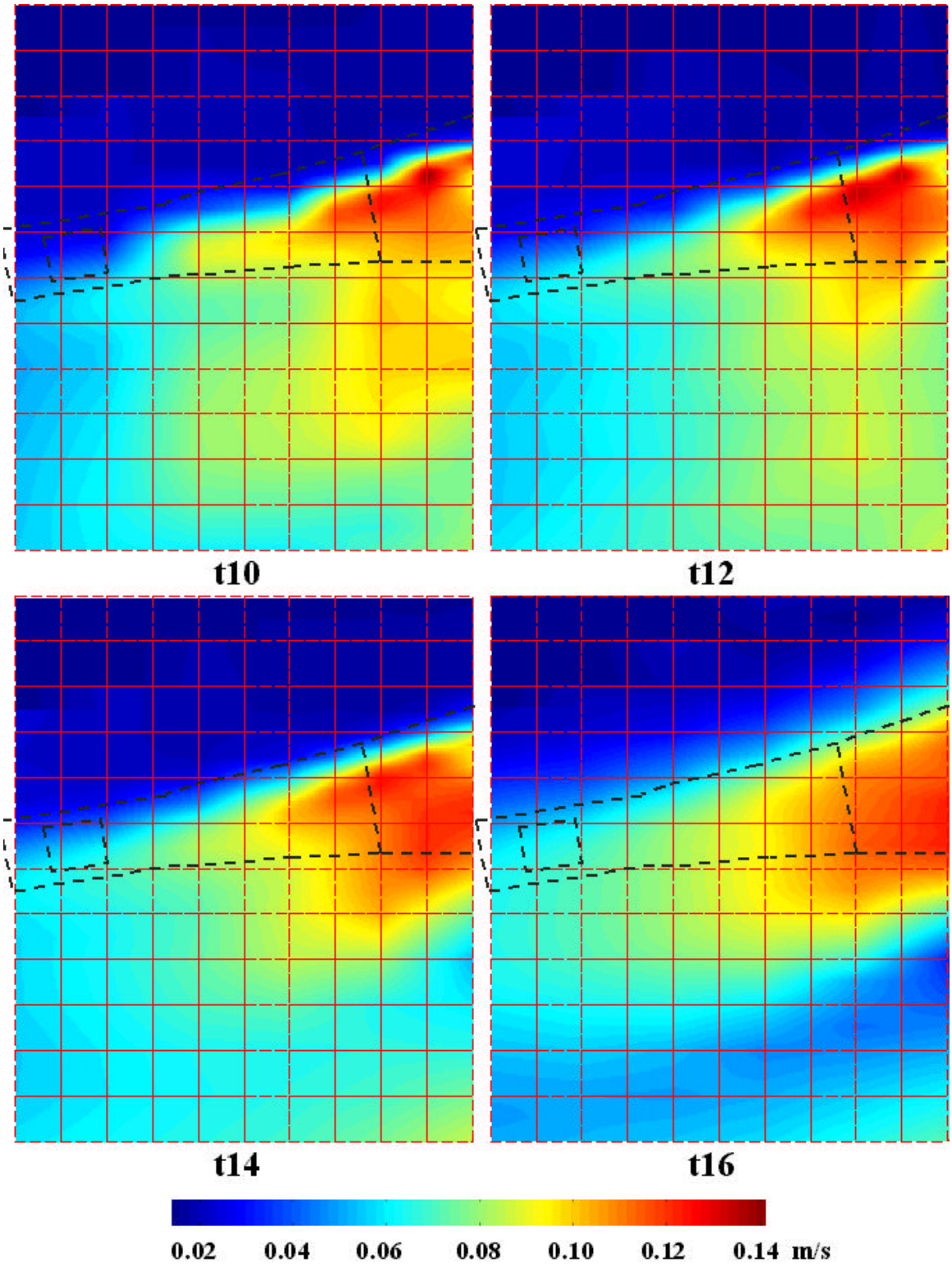

Figure 43: Distributions of 10-20 kHz component of RMS flow fluctuation.

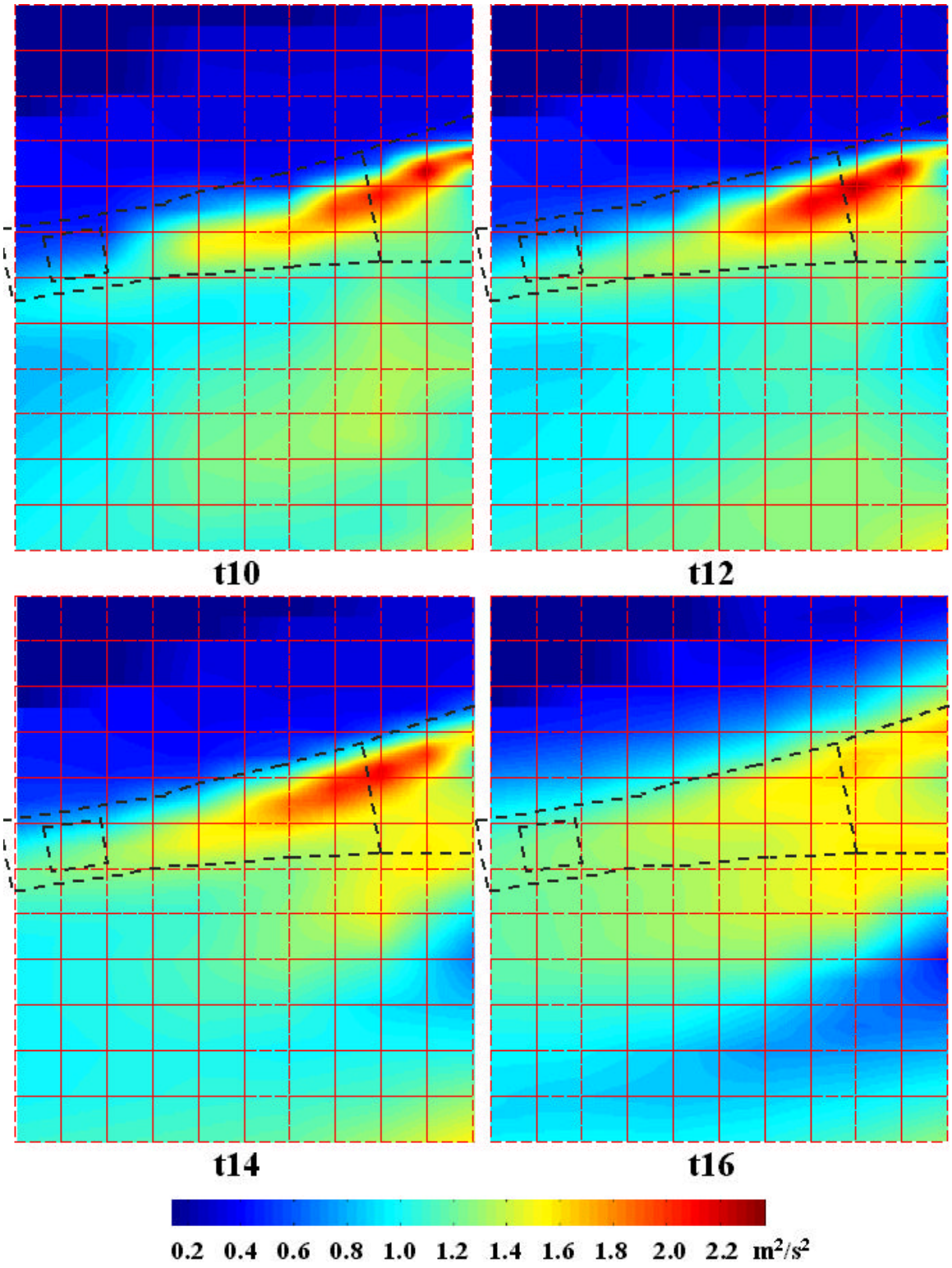

Figure 44: Distributions of 10-20 kHz component of RMS dynamic head fluctuation.

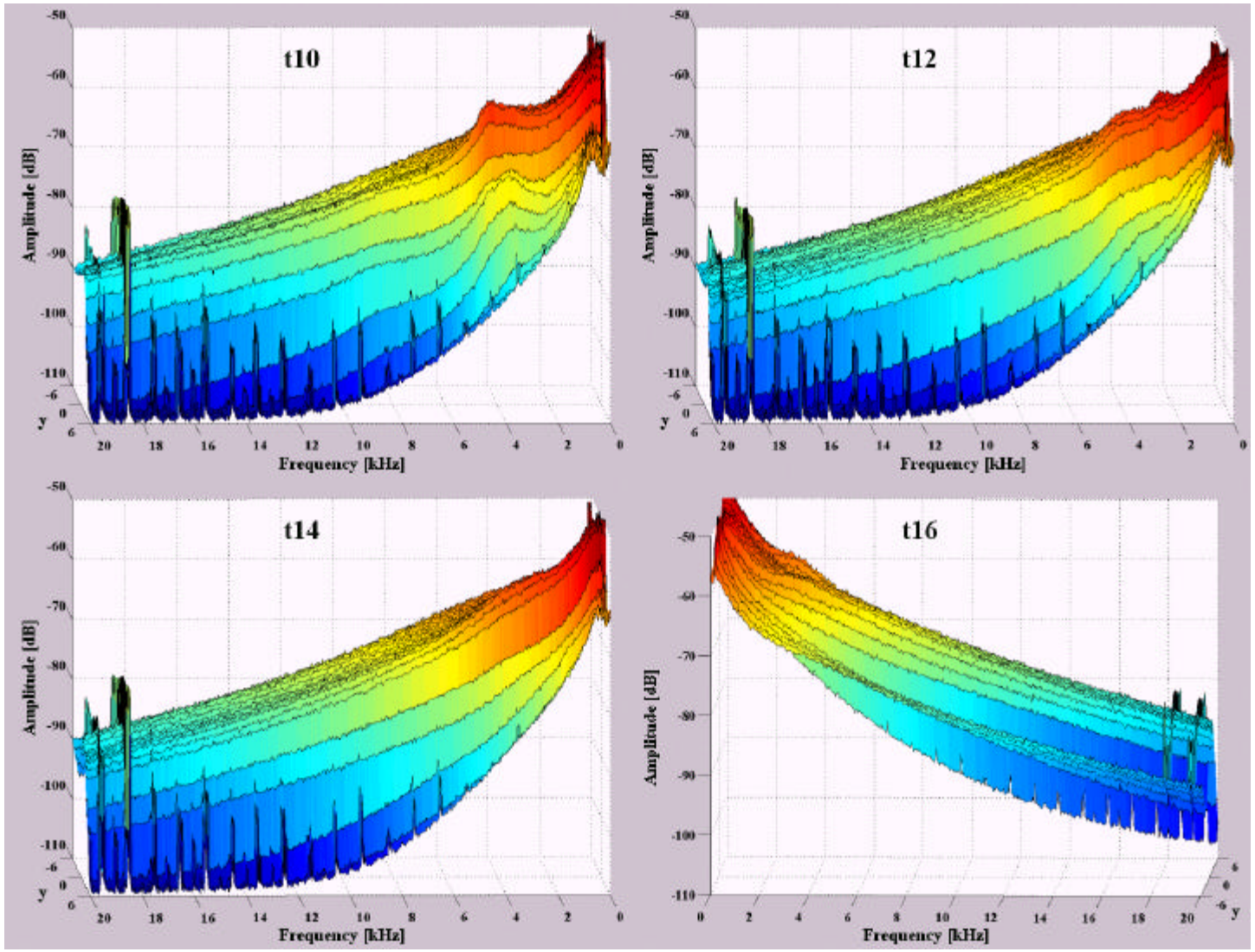

Figure 45: Flow fluctuation power spectra at $x = 2\ mm$.

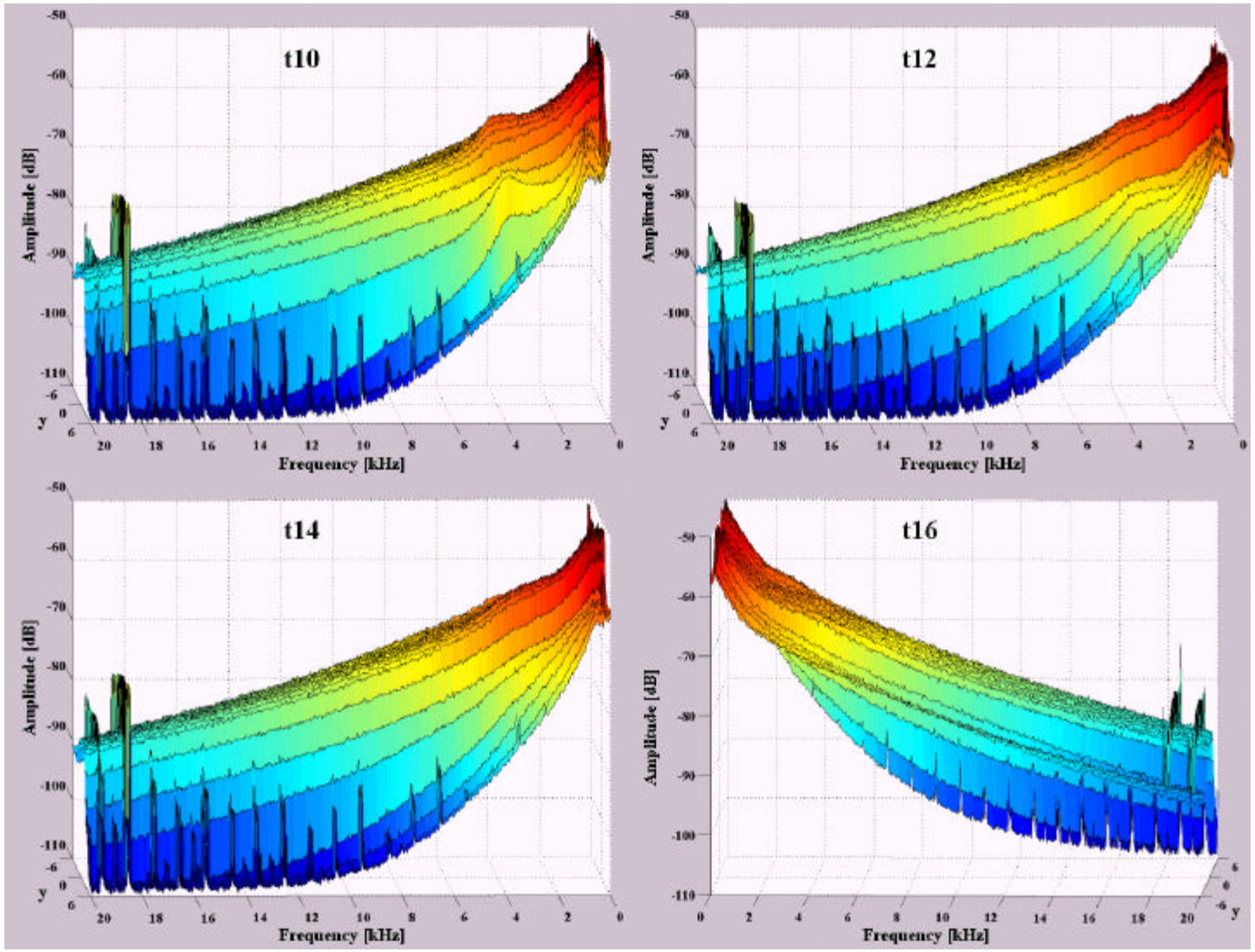

Figure 46: Flow fluctuation power spectra at $x = 4\ mm$.

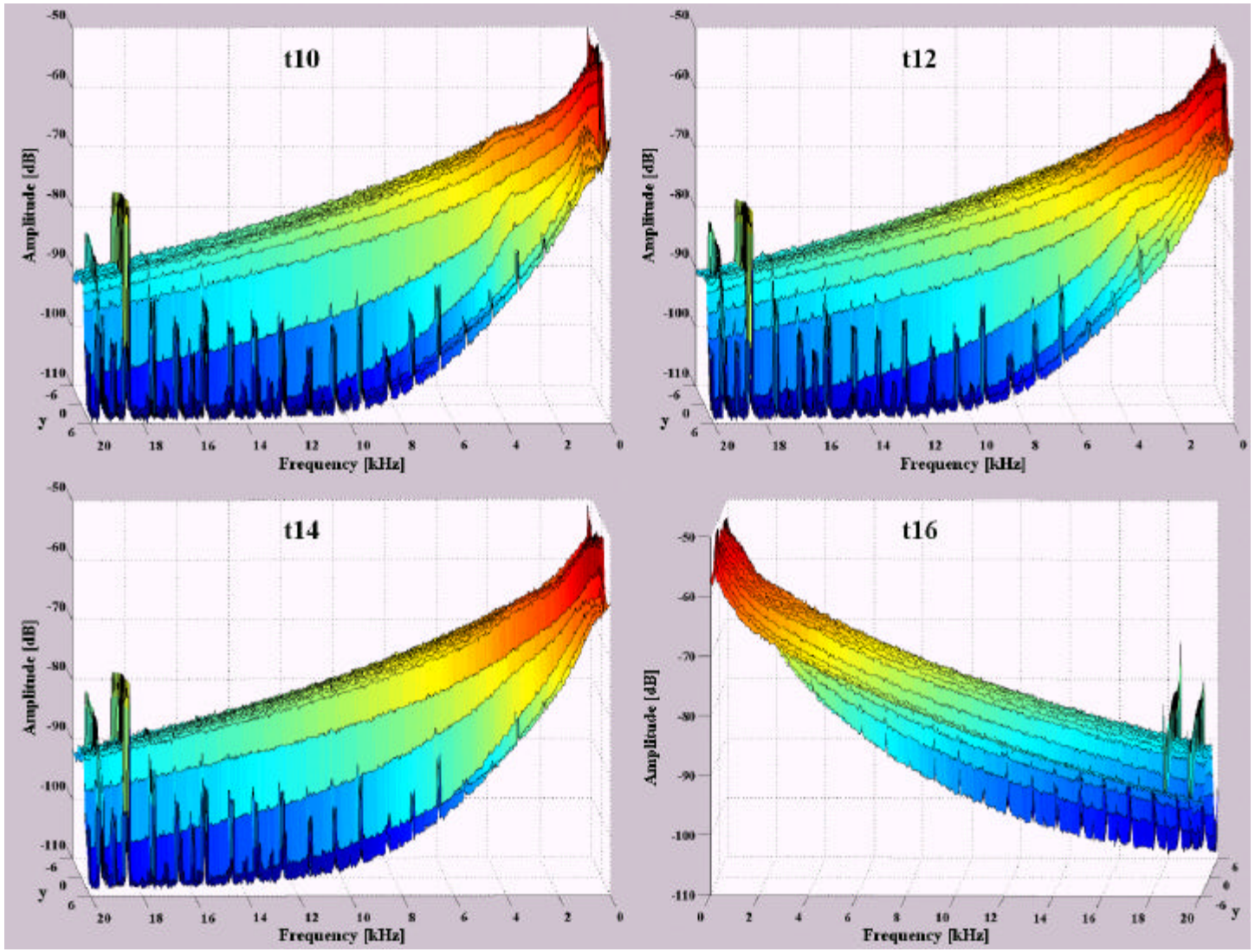

Figure 47: Flow fluctuation power spectra at $x = 6\ mm$.

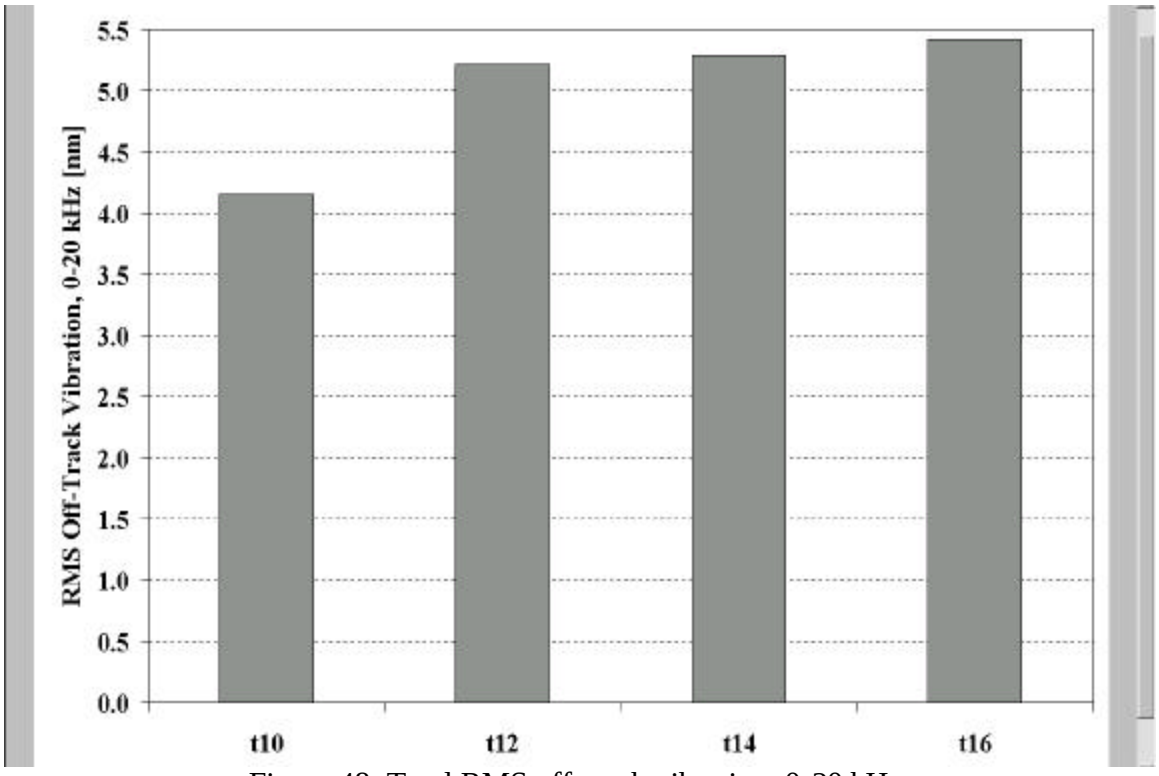

Figure 48: Total RMS off-track vibration, 0-20 kHz.

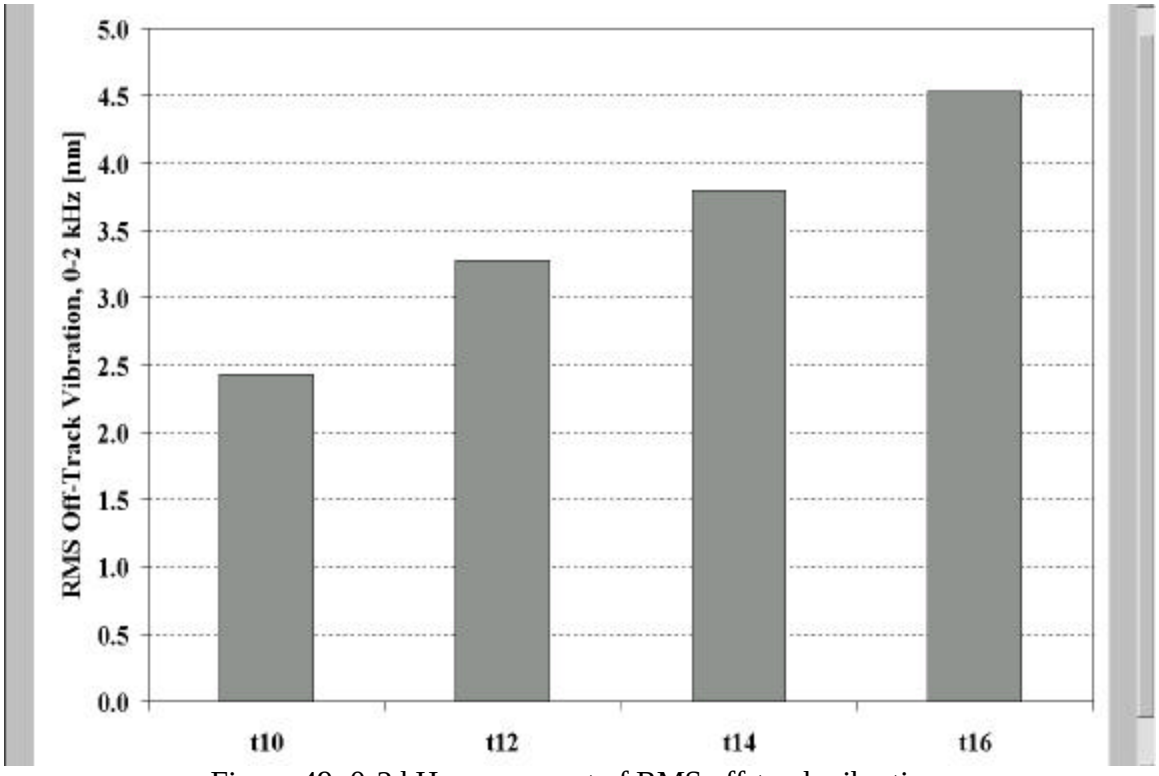

Figure 49: 0-2 kHz component of RMS off-track vibration.

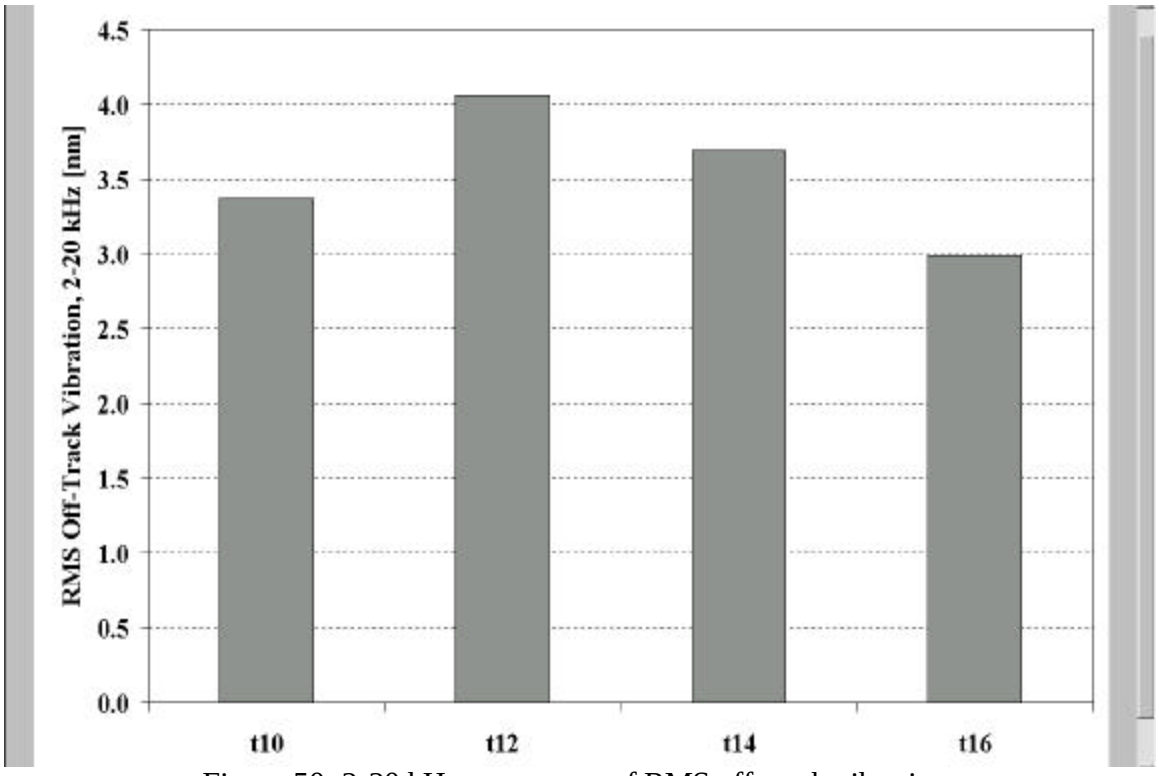

Figure 50: 2-20 kHz component of RMS off-track vibration.

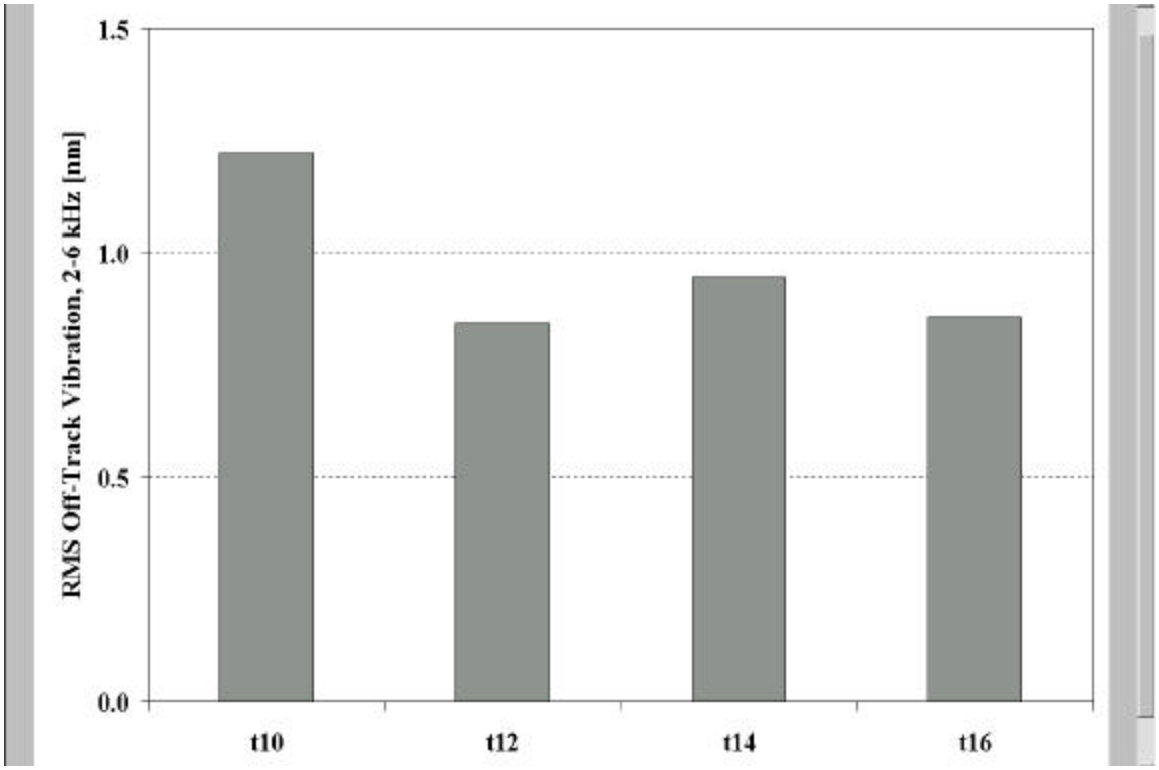

Figure 51: 2-6 kHz component of RMS off-track vibration.

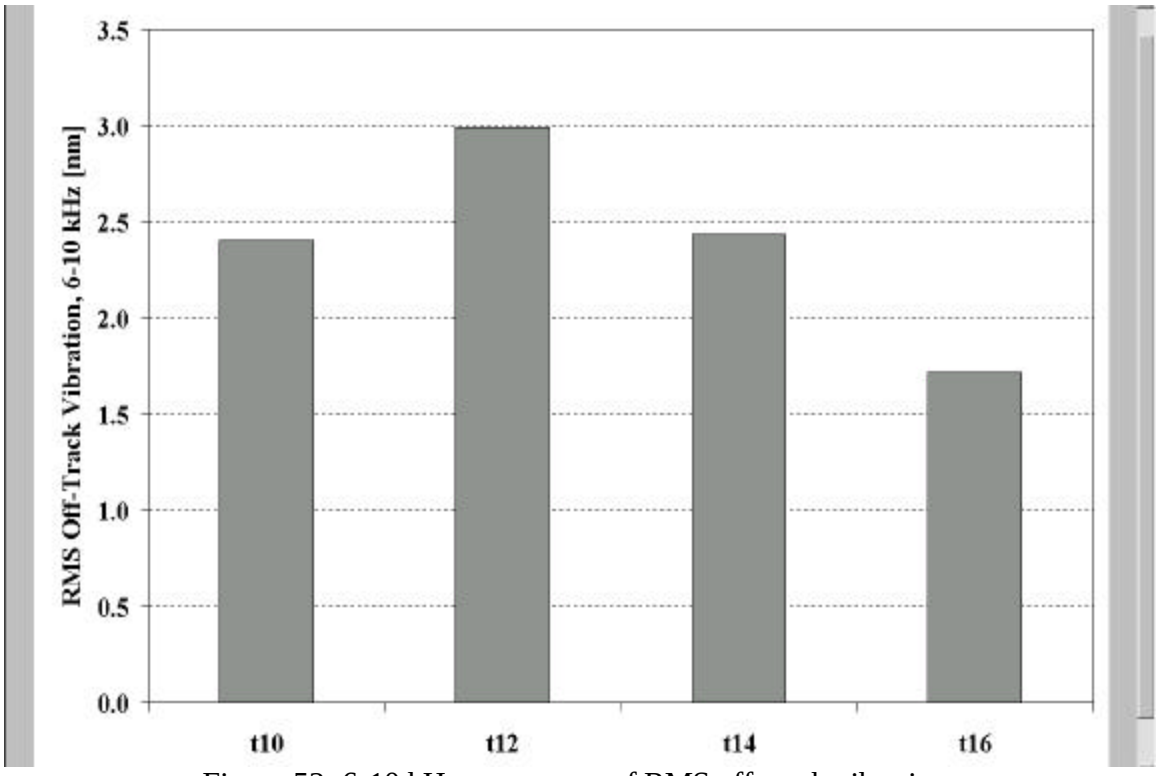

Figure 52: 6-10 kHz component of RMS off-track vibration.

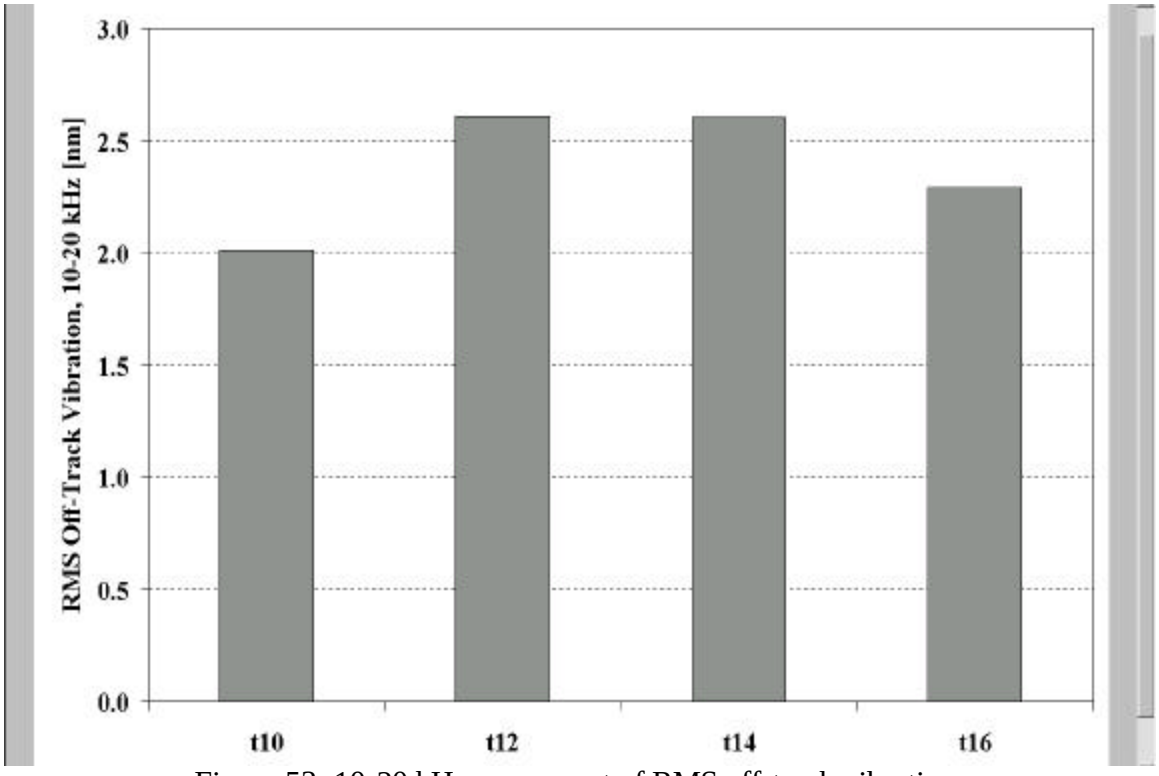

Figure 53: 10-20 kHz component of RMS off-track vibration.